CrossMark

Experimental assessment of the Tenti S6 model for combustion-relevant gases and filtered Rayleigh scattering applications

Thomas A. Mcmanus[1] · Ignacio Trueba Monje[1] · Jeffrey A. Sutton[1]

Abstract

Accurate descriptions of Rayleigh–Brillouin scattering (RBS) spectra for gas-phase species are important in light scattering measurement techniques including filtered Rayleigh scattering (FRS). The current manuscript targets evaluation of the well-known Tenti S6 model for calculating the RBS spectra for combustion-relevant species over a broad range of temperatures with relevance towards FRS applications in reacting flows. In this work, testing of the Tenti S6 model was performed by comparing measured FRS signals to synthetic FRS signals generated through the combination of the Tenti S6 model and an experimentally verified I_2 absorption model. First, temperature-dependent FRS signals were measured for a number of individual gases including Ar, N_2, O_2, CH_4, H_2, CO, and CO_2 from 300 to 1400 K. Comparisons between the measurements and synthetic FRS signals show excellent agreement ($< 4\%$ average difference) over the full temperature range. For pure CO_2, rotational Raman scattering effects must be taken into account when comparing measured and synthetic FRS signals. FRS measurements in binary mixtures were performed to assess the commonly used (but not verified) assumption that the total FRS signal from a mixture can be treated as the mole fraction-weighted average of the FRS signals from each component. Measured FRS signals in mixtures with large variations in both molecular weight and Rayleigh scattering cross section show a linear relationship with constituent mole fraction, indicating that this assumption is valid within the kinetic regime. Finally, FRS measurements were performed in near-adiabatic H_2/air and CH_4/air flames. Comparisons between measured and synthetic FRS signals show excellent agreement over a broad range of equivalence ratios (ϕ), which includes a temperature range of $1100 < T(K) < 2400$ and large relative changes in species mole fractions. Overall, the results indicate that the predicted RBS lineshapes calculated using the Tenti S6 model are sufficiently accurate in the context of FRS measurements for the species and temperatures evaluated.

1 Introduction

Laser light scattering is a widespread tool used within the atmospheric science, fluid dynamics, and combustion communities to measure gas properties such as temperature, density, and velocity. Light scattering from gases can be traced back to Lord Rayleigh's classical derivation using Maxwell's formulism of electromagnetism [1]. Light scattering due to density (and hence refractive index) fluctuations arises from both temperature (entropy) and pressure fluctuations. The pressure fluctuations manifest as acoustic waves within the medium and the interaction between

light and the sound waves results in "Brillouin scattering" [2]. The spectrum describing light scattering caused by the density fluctuations is called Placzek trace scattering [3], which consists of a central elastic Gross or Landau–Placzek line and the set of Brillouin doublets which are Doppler shifted from the central peak due to the motion of the scattering acoustic wave. The collective process, along with the rotational Raman Q-branch, yields the Cabannes line and is commonly described as 'elastic scattering'. The combination of the Cabannes line and Stokes and anti-Stokes (S/AS) rotational Raman scattering yields the total quantity referred to as "Rayleigh scattering", while the designation of "Rayleigh–Brillouin scattering" (RBS) typically is reserved for the Cabannes line only. The contribution of rotational Raman scattering to the total scattering typically is small ($< 2\%$), but there are exceptions as described below.

A key parameter describing the Cabannes line or RBS spectral lineshape is the non-dimensional y parameter, which

✉ Thomas A. Mcmanus
  mcmanus.46@osu.edu

1 Mechanical and Aerospace Engineering Department, Ohio State University, 201 W. 19th Ave., Rm N350, Columbus, OH 43210, USA

is defined as the ratio of scattering wavelength to the mean free path [4, 5]:

$$y = \frac{nk_\mathrm{B}T}{k_\mathrm{s}\mu v_\mathrm{o}}, \tag{1}$$

where n is the gas number density, k_B is the Boltzmann constant, T is the gas temperature, k_s is the magnitude of the scattering wave vector, μ is the shear viscosity, and v_o is the $(2k_\mathrm{B}T/M)^{1/2}$ is the most probable thermal velocity. When $y \ll 1$ (Knudsen regime), the density is low enough such that the mean free path between collisions is much larger than the scattering wavelength. In this regime, the scattering is due to individual molecules only and the effects of pressure fluctuations are negligible. In this manner, the RBS lineshape is described by a single Gaussian distribution corresponding to a Maxwell velocity distribution of the molecules. For $y \gg 1$ (hydrodynamic regime), the mean free path between collisions is much smaller than the scattering wavelength and thus the gas can be treated as a continuum. Within this regime, the collective scattering effects can be solved using the Navier–Stokes equations which results in RBS lineshapes that are well described by the sum of three Lorentzian functions with three distinct peaks (the central Gross peak and the two Brillouin sidebands).

In the kinetic regime ($0.3 \lesssim y \lesssim 3.0$), neither a Gaussian (individual particle approach) nor a set of Lorentzian functions (continuum approach) can be used to describe the RBS lineshape and the Boltzmann equation must be used to describe the scattered light spectrum by solving for density fluctuations. However, the solution of the Boltzmann equation requires knowledge of the collisional cross sections between molecules, which, in general, is not available, thus requiring accurate models to describe the RBS spectral lineshape. The most common set of models describing the RBS spectra of individual molecules are the Tenti S6 and S7 models [4, 5]. These models describe the scattering profiles based on approximate solutions of the linearized Boltzmann equation where the collision integral is approximated using the Wang Chang and Uhlenbeck approach [6]. For the S6 (or S7) model, the collision operator is truncated after six (or seven) terms (or moments) and the coefficients of the basis functions are determined from transport coefficients including shear viscosity (μ), bulk viscosity (μ_B), thermal conductivity (κ), and internal specific heat capacity (c_int).

Accurate knowledge or modeling of the RBS spectral lineshape is important for many fields including recent advancements in LIDAR-based measurements for wind speed and temperature distributions in the Earth's atmosphere [7, 8]. This particular application has prompted high-resolution RBS profile measurements from molecular gases including N_2, O_2, CO_2, and air [e.g., [9–14]]. For example, Vieitez et al. [9] measured both coherent and spontaneous

RBS profiles of N_2 and O_2 at room temperature and pressures ranging from 1 to 3 bar. Ma et al. [10] measured RBS profiles of N_2 and air at temperatures ranging from 250 to 340 K and pressures ranging from 1 to 3 bar. Witschas et al. [11] measured RBS spectra for N_2, dry air, and humid air over a temperature and pressure range of 295–301 K and 0.3–3 bar, respectively, while Gu et al. [12] examined the RBS spectra of CO_2 at pressures of 2–4 bar at room temperature conditions. Using an improved excitation and detection system, Gu and Ubachs and Gu et al. [13, 14] measured RBS spectra of N_2, O_2, and air at pressures ranging from 0.6 to 3 bar and at temperatures ranging from 250 to 340 K. Under these conditions ($0.4 \lesssim y \lesssim 1.7$), it was observed that the Tenti S6 model performs very well with deviations between the modeled RBS spectra and measurements at the few percent level. It also has been observed that the S6 model generally outperforms the S7 model. Finally, it is noted that after surveying the literature, the majority of measurements are confined to air constituents (i.e., O_2, N_2, or CO_2) and over a relatively limited range of temperatures.

For fluid dynamics and combustion measurements, knowledge of the RBS spectrum is a key component in a diagnostic referred to as filtered Rayleigh scattering (FRS) (e.g., [15, 16]). FRS is a modification of laser Rayleigh scattering (LRS), which describes the quasi-elastic scattering of laser light from small particles, i.e., atoms and molecules. In FRS, a spectrally narrow laser is used in conjunction with an atomic or molecular vapor filter placed in front of a camera. This setup is used to discriminate between unwanted scattering that is resonant with the laser (i.e., surface and/or particulate) and the desired scattering from gas-phase species that is broadened due to the RBS process. Figure 1 shows a graphical representation of the FRS approach when using a narrowband Nd:YAG laser and a molecular iodine filter. As shown in Fig. 1, iodine makes an excellent filter in conjunction with a narrowband Nd:YAG laser, where the I_2 absorption spectrum acts as a suitable medium for absorbing unwanted surface/particle scattering, while transmitting a portion of the broadened RBS spectrum. This allows the possibility of FRS facilitating gas-phase measurements in the presence of otherwise, interfering scattering media. For example, FRS has been used previously in non-reacting fluid environments to measure average velocity, pressure, and temperature in compressible flows [17], turbulent jets [18], and ducted gas flows [19]; trajectory and mixing properties in buoyant jets [20]; temperatures in boundary layers near surfaces [21] and fuel vapor/air mixing in droplet/gas regions of an evaporating spray flow [22].

The most common application of FRS in combustion and plasma systems is the deduction of temperature in environments with high levels of interference (e.g. [23–28]). For example, Hofmann and Leipertz [23] first demonstrated FRS thermometry in lightly sooting
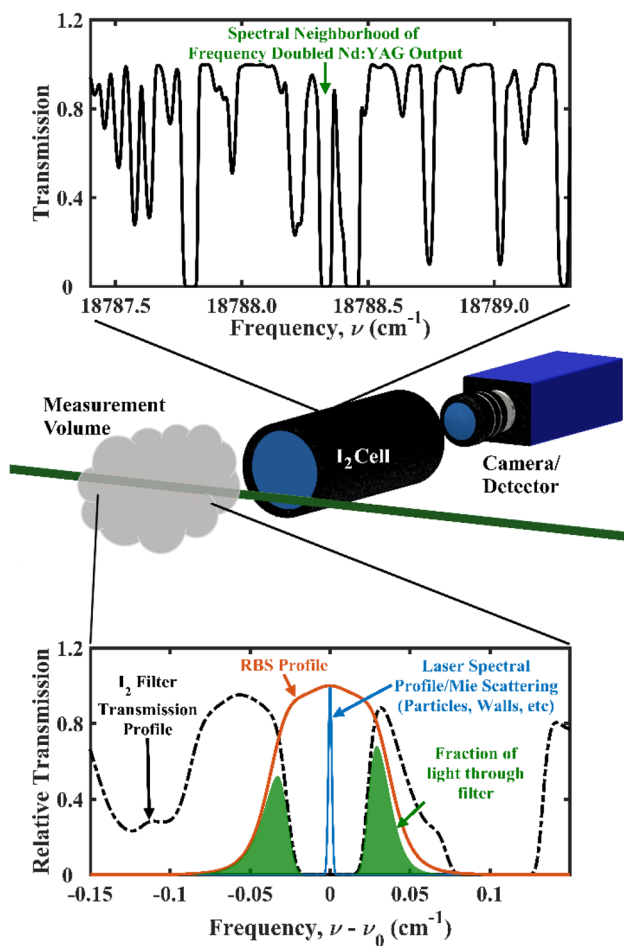
Fig. 1 FRS concept using an Nd:YAG laser and molecular iodine filter. Modeled I_2 spectrum (top). The feature marked with an arrow is used in the present work for FRS measurements. Potential application of imaging FRS signal within a particle laden flow (middle). Overlap of the I_2 filter profile with particle scattering, and an example RBS profile from gas-phase molecules (bottom)

premixed flames [26], and temperature in non-premixed flames [28].

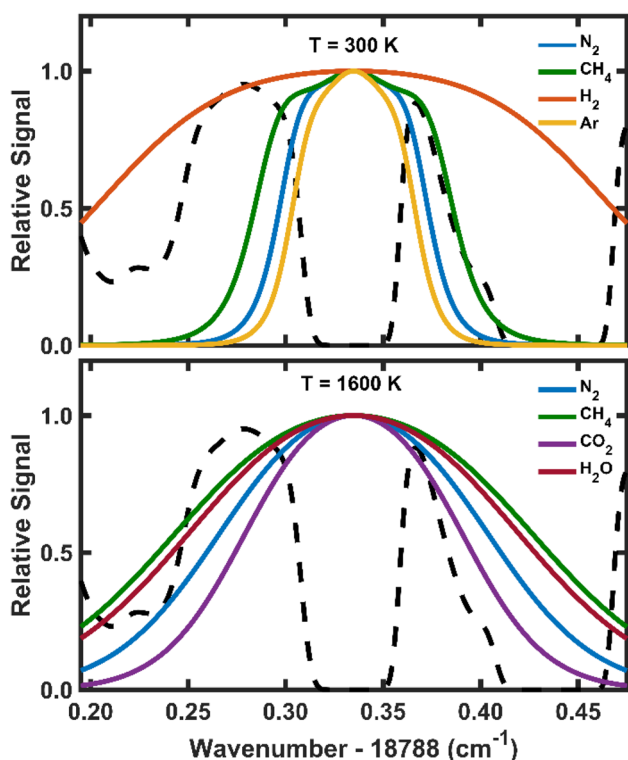The measured FRS signal from a single species i can be written as

$$S_{\text{FRS},i} = CI_0 n_i \psi_i, \tag{2}$$

where C is a constant associated with the collection optics and imaging system, I_0 is the incident laser intensity, n_i is the number density of species i and ψ_i is an FRS specific variable which can be expressed as

$$\psi_i = \sigma_i \int_\nu \mathcal{R}_i\big(P, T, V, \theta, \nu_r\big)\tau_{I2}(\nu)\mathrm{d}\nu. \tag{3}$$

In the above equation, σ_i is the differential Rayleigh scattering cross section for species i, $\mathcal{R}_i\big(P, T, V, \theta, \nu_r\big)$ is the RBS lineshape for species i, $\tau_{I2}(\nu)$ is the frequency-dependent transmission of the molecular I_2 filter, ν is the spectral frequency over which the RBS light and I_2 transmission bands are distributed, and $\nu_r = \nu - \nu_o$ is a frequency referenced to the center laser frequency. In Eq. (2), it has been assumed that S/AS rotational Raman scattering contributes negligibly to the collected signal. It is noted that in addition to being a function of gas composition, the RBS lineshape is a function of the flow velocity (V), the laser frequency (ν_0), observation angle (θ), temperature (T), and pressure (P). Equations (2) and (3) show that quantitative interpretation of the measured FRS signal requires knowledge of the RBS lineshape of each species. For example, Fig. 2 shows an example of RBS profiles calculated for various combustion-relevant species at 300 K and 1600 K. It is noted that the RBS profiles vary significantly across species, even at 1600 K, which is presumably dominated by Doppler broadening. Figure 3 shows the calculated y parameter (Eq. 1) as a function of temperature for seven common combustion-relevant species at 1 atm. It is clear from the results that for a large temperature range, the scattering is in the kinetic regime, which requires detailed modeling of the RBS spectrum as opposed to simplified analytic expressions (Gaussian or Lorentzian). It also is noted that at higher pressures, the scattering will fall within the kinetic regime for an even larger range of temperatures.

A complication with FRS-based measurements in combustion environments is that at any point in space there may be a mixture of species such that the FRS signal arises from the net effect of the local species within the mixture. Strictly speaking, this accounts to replacing $\mathcal{R}_i$ in Eq. (3) with a RBS spectrum from the gas mixture, $\mathcal{R}_{\text{mix}}$. A kinetic description of the RBS spectrum from gas mixtures (analogous to the Tenti S6 model for single species) is very difficult because there is a need for many additional transport coefficients describing inter-species transport that are not known. Simpler kinetic models, where mixture constituents interact as "hard spheres" have been developed by Marques

premixed flames, where scattering from soot particles renders the majority of common thermometry approaches unusable. Subsequently, Elliot et al. [24], Most and Leipertz [25], and Most et al. [26] demonstrated simultaneous temperature and velocity measurements in laminar and turbulent flames using simultaneous FRS and particle imaging velocimetry (PIV). Similar to sooting flames, scattering interference from the tracer particles necessary for PIV creates significant challenges for the majority of thermometry approaches. For particle-laden flames (whether sooting or seeded), scattering from particles is absorbed by the I_2 filter and the portions of the transmitted gas-phase FRS signal are used to determine temperature. Following these initial demonstrations, FRS-based thermometry has been used to determine temperature in weakly ionized plasmas [27], turbulent heat flux in

Fig. 2 Example lineshapes (solid) overlapping with I_2 spectra (dashed) in the neighborhood of 532 nm. $T = 300\,\text{K}$ and $P = 760\,\text{Torr}$ (top). $T = 1600\,\text{K}$ and $P = 760\,\text{Torr}$ (bottom). The I_2 absorption spectrum is calculated at $P = 1\,\text{Torr}$ with a cell absorption length of 25 cm
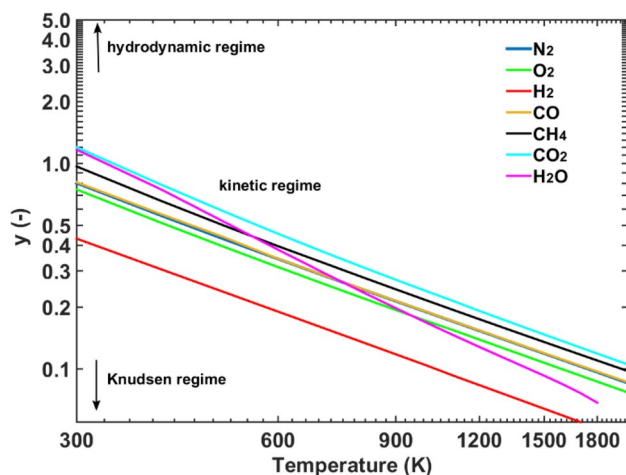
Fig. 3 Calculated y parameter for several combustion-relevant species as a function of temperature at $P = 1$ atm. Calculations are performed for 532-nm excitation and an angle of 90° between the incident light and the detector

et al. [29–31] to describe binary mixtures. Comparisons to experimental results [9, 32, 33] show that this type of model works well at higher pressures for noble gas mixtures but not

for mixtures at low pressures and for species with internal degrees of freedom. While the Tenti model is not designed to describe RBS lineshapes of mixtures, one approach that has been used to model the RBS lineshape of air (a mixture of O_2, N_2, and other trace species) is to treat air as a fictitious gas with effective transport coefficients. This approach has yielded good agreement between model predictions and measurements in both dry and moist air [13, 14]. For combustion systems it is not possible to represent the species mixture as a single fictitious species since the number of species present is too large and changes in space and time due to mixing, diffusion, and reaction.

For FRS applications, it is more important to describe the net effect of the various mixture constituents as opposed to accurately determining $\mathcal{R}_{\text{mix}}$. Perhaps an effective approach is to represent the measured FRS signal from a mixture in an analogous manner to that of traditional LRS; that is, the measured signal is treated as a mole-weighted average of the FRS signal from each individual component in the mixture:

$$S_{\text{FRS, mix}} = CI_0 n \Sigma_i X_i \psi_i, \tag{4}$$

where X_i is the mole fraction of species i. It is expected that this formulation is valid for gases in the dilute limit where there is little interaction between species. However, it has been assumed previously in the kinetic regime (e.g., [22, 28]), but has not been tested experimentally. In the current work, this assumption is assessed initially by examining the FRS signal for a series of binary mixtures at atmospheric temperature and pressure conditions.

The current manuscript presents results targeted at testing the Tenti S6 model [5] for several combustion-relevant species at elevated temperatures with relevance towards accurate FRS thermometry measurements in flames. In this work, a different approach is taken as compared to previous studies that have directly measured the species-specific RBS lineshapes at a few select temperatures (e.g., [9–14]). We perform indirect testing of the Tenti S6 model by comparing measured FRS signals from various species as a function of temperature to synthetic FRS signals generated from the combination of the Tenti S6 RBS model and the experimentally verified I_2 transmission model from Forkey et al. [34] [see Eqs. (2) and (3)]. As shown from Eqs. (2) and (3), if the Rayleigh scattering cross section and I_2 transmission are known accurately, then agreement between measured and synthetic FRS signals implies a reasonably accurate representation of the RBS lineshape using the Tenti S6 model. Similarly, disagreement between measured and synthetic FRS signals corresponds to inaccurate modeling of the RBS lineshape. Thus a comparison of the measured and synthetic FRS signals provides a suitable "macroscopic" assessment of the accuracy of the Tenti S6 model over a broad range of species and temperatures. Additionally, we present results in gas mixtures at atmospheric conditions to assess a simple
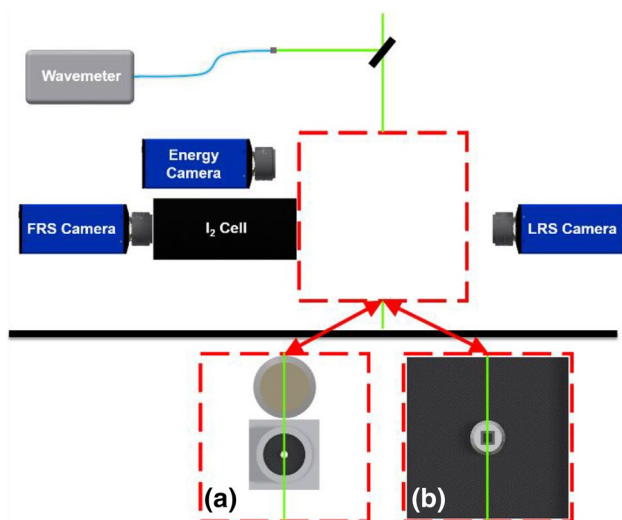
Fig. 4 Experimental setup for simultaneous FRS and LRS measurements used for the assessment of the Tenti S6 RBS spectral model. Three cameras image laser scattering over two different experimental flow setups. **a** Temperature-dependent, measurements for individual species and binary mixtures at room temperature. **b** Setup for Hencken flame measurements

(but not previously tested) assumption that the FRS signal from a gas mixture is simply a mole fraction-weighted average of the individual species contributions. Finally, comparisons between measured and synthetic FRS signals from near-adiabatic H_2/air and CH_4/air flames are performed over a broad range equivalence ratios, corresponding to several mixture compositions and temperatures.

2 Experimental approach

All FRS measurements are performed using a common base experimental setup. Figure 4 shows a general schematic of the experimental layout with insets depicting the different flow configurations used for various assessments as described below. The laser source is an injection-seeded, frequency doubled, Q-switched, Nd:YAG laser operating at a repetition rate of 10 Hz. The nominal pulse energy for the measurements was ~ 160 mJ/pulse and the pulse duration was ~ 7 ns. The laser was tuned to a spectral frequency of 18788.335 cm^{-1}, which corresponds to the R56 (32,0) and P159(39,0)/P103(34,0)/P53(2,0) transitions of the $B \leftarrow X$ electronic system of iodine. Prior to entering the measurement volume, a small portion of the laser beam is sent to a high-resolution wavemeter (High Finesse WSU30) with an accuracy of 30 MHz to monitor the wavenumber for each laser pulse. The wavemeter is automatically calibrated twice every hour by a fiber-optic-coupled, frequency-stabilized, He–Ne laser operating near 632 nm. The 532-nm output

from the Nd:YAG laser is then directed towards the test section and focused using a 750-mm focal length spherical lens.

Three scientific-grade CCD cameras without image intensifiers are used in the experiment. The first camera (labeled the "FRS Camera" in Fig. 4) is placed behind an I_2 cell to collect the temperature- and species-dependent FRS signals. A high transmission, 532-nm bandpass filter (BPF) is placed between the CCD camera and the I_2 cell to minimize any extraneous light signals. The I_2 cell is 248 mm long and 76 mm in diameter. It is a starved-cell design filled with a sidearm temperature of approximately 39 °C, corresponding to an I_2 partial pressure of 0.96 Torr. The main body of the cell is surrounded by electrical resistance heating tape and operated at a super-heated temperature of 341 K to ensure no I_2 vapor recrystallizes to the solid phase within the filter cell during operation. The cell is maintained at the specified temperature by a digital temperature controller (Cole-Parmer DigiSense) which has a quoted accuracy of 0.1 K. The second camera is used to capture traditional laser Rayleigh scattering from the flow of interest (labeled the "LRS Camera" in Fig. 4). For the heated flows and near-adiabatic flame measurements the LRS measurements are used to determine the local gas temperature, which is used in the analysis of the FRS signals and the corresponding comparison to modeled FRS predictions. For the binary mixture measurements, the LRS measurements are used to determine the component mole fractions in situ. The LRS camera is focused over the same field-of-view as the FRS camera. The third camera is focused over a uniform air flow issuing from a matrix burner (labeled the "Energy Correction" camera in Fig. 4) to monitor and correct for shot-to-shot laser energy fluctuations.

2.1 Temperature-dependent, single species measurements

A straightforward experimental configuration is implemented to generate the conditions necessary for the temperature-dependent FRS measurements of each gaseous species. An electrically heated jet surrounded by an inert N_2 coflow is used, where the laser measurements are performed in the potential core of the jet to ensure that the gas-phase scattering only originates from the single species of interest (i.e., no mixing of multiple streams). The approach avoids complications and that arise when using typical optical test cells for high-temperature test conditions, such as uniform heating, limitations on peak temperatures (due to heat transfer), and interference from windows. Without the latter consideration, the current approach allows for a straightforward temperature measurement of each single species via traditional LRS. Two inline heaters are used separately to achieve the desired temperature range. The first heater is a Tutco HT050 rated for a maximum wattage of 450 W and is used to access the low to mid-range temperatures of

300–900 K. The second heater is an Osram-Sylvania Series III air heater rated for a maximum wattage of 2050 W and is used to reach the upper temperature ranges for the current work (~ 900 K to ~ 1400 K). The inline heaters are oriented in a vertical orientation and placed directly into the inert N_2 coflow, such that the circular outlet of the inline heater acts as the jet exit. The diameters of the two heaters, and hence the jet exit diameters, are 13.7 mm and 15 mm, respectively. The gases examined include N_2, Ar, air, CO_2, H_2, CH_4, and CO. The coflow of N_2 not only provides isolation from the surroundings (i.e., prevention of dust for LRS), but also helps prevent autoignition from occurring when measuring the FRS signals for the fuels at high temperatures. For the current measurements, the flow rates entering the inline heater range from 26 to 37 standard liters per minute (SLPM), depending on the particular gas. The flow rates are fixed for a particular gas for the full range of temperatures, corresponding to Reynolds numbers (Re) based on jet exit diameter of 310–5700, covering both laminar and turbulent jet conditions. With the exception of H_2, all operating conditions correspond to $Re > 1200$ and all cases are turbulent for $T < 400$ K.

To ensure the FRS signals originate from a single species in this configuration, the measurements must be performed within the potential core of the jet. The potential core of a jet does not experience any momentum nor mass transfer with the surrounding region and thus does not mix with the surroundings. Thus, the species composition exiting the tube remains constant within the potential core. In general, the potential core length is a non-monotonic function of Re for laminar flow conditions with no analytical solution for variable-density flows. However, previous works have shown for $Re \gtrsim 300$, the potential core of the laminar jet is greater than that of the turbulent jet (e.g., [35, 36]) which is not dependent on Re. In this manner, for any given temperature, the potential core of a turbulent jet case can be considered as the shortest possible potential core length that could be encountered during testing and can be used to determine the appropriate measurement location. The length of the potential core (x_{pc}) of turbulent jets can be estimated from known turbulent jet scaling laws [37, 38] as

$$x_{pc}/d \leq 5.4 \left(\frac{\rho_i}{\rho_\infty} \right)^{\frac{1}{2}}, \qquad (5)$$

where d is the jet exit diameter, ρ_i is the jet gas density, and ρ_∞ is the coflow gas density.

Using the above equation, the potential core was estimated across the range of temperatures tested for each gas species, assuming it remained turbulent for all cases (which provides the most restrictive guidelines on necessary measurement location). Figure 5 shows the estimated potential
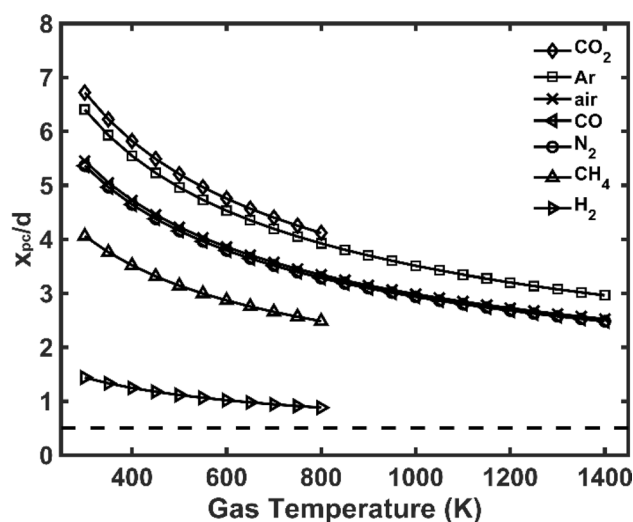
Fig. 5 Estimated potential core lengths of the jet for various species as a function of gas temperature. The nitrogen coflow is assumed to be 296 K

core length normalized by the tube diameter for turbulent jets of each gas species as a function of temperature. For all gases, the calculated potential core length decreases with increasing gas temperature due to the change in the jet density. Based on these results, a measurement location of $x/d = 0.5$ was targeted, which should ensure than the LRS/FRS measurements are performed within the jet potential core regardless of operating condition. The measurement at $x/d = 0.5$ also is sufficiently far enough downstream from the burner surface (6.85 and 7.5 mm, respectively, for the two heaters) such that no stray light from surface scattering was observed. The measurement location is shown in Fig. 5 as a dashed line. For all test cases, the temperature within the potential core is determined via LRS from.

$$T_{LRS} = T_{ref} \times S_{ref}/S_{LRS,i}(T), \qquad (6)$$

where $S_{LRS,i}(T)$ is the measured LRS signal of species i at temperature T, T_{ref} is a reference temperature, which is 296 K for all cases considered in this work, S_{ref} is the measured LRS signal at T_{ref}, and it is assumed that the Rayleigh scattering cross section does not vary as a function of temperature[1].

Given that the internal structure of the inline heaters is more complex geometrically than a simple circular tube, the jet flow structure was occasionally perturbed such that small amounts of fluid from the coflow entered into the

---

[1] In Ref. [41]. the temperature dependence of the Rayleigh scattering cross sections (σ_i) were reported at 355 and 266 nm. No temperature dependence was reported at 532 nm because the temperature variation of σ_I over the temperature range of 300–1500 K was less than the uncertainty (2%) of the measurements.
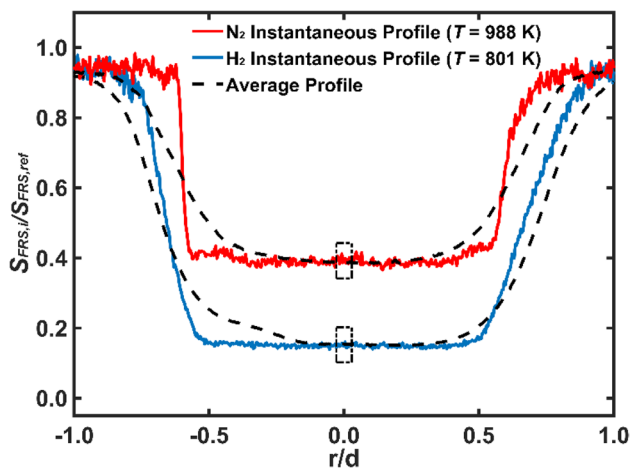
Fig. 6 Example relative FRS signal profiles from a heated jet. Instantaneous profile shown in red and blue solid lines, while the corresponding mean profiles are shown in black dashed lines. The small, dashed box indicates the region where the FRS and LRS signal ratios are determined for analysis

measurement region and thus contaminated the measurement. To mitigate the effects of these rare occurrences, a post processing algorithm was applied to the FRS and LRS signal profiles to flag samples which had been contaminated. These particular measurements were then discarded such that the analysis and statistics were applied only to acceptable samples. The algorithm to filter out contaminated samples involved examining the FRS and LRS profiles within a central region in the jet and rejecting the samples with a percent difference between the maximum and minimum value within that region that exceeded a user-defined threshold. For all of the gases and temperature conditions examined, the majority of the samples were considered "acceptable" and thereby provided large sample sizes for determining the mean FRS signal ratio and gas temperature via LRS.

An example of two "acceptable" instantaneous and the corresponding average FRS signal profiles is shown in Fig. 6. The relative FRS signal, $S_{FRS,i}/S_{FRS,ref}$ is shown, where $S_{FRS,i}$ represents the measured FRS signal for a particular species and $S_{FRS,ref}$ is a reference condition, which is pure N_2 at $T = 296$ K. The two conditions shown are at elevated temperatures and in particular, the $T = 801$ K H_2 jet is the most challenging case in terms of shortest potential core ($Re \approx 300$) and potential buoyancy effects. The example relative FRS signal profiles show some distinct features that give confidence in the measurement approach. First, for the instantaneous profiles, there is a distinct flat region that spans a radial distance of one jet diameter, which is the expected result when in the potential core near the jet exit. Second, the FRS profiles approach a value of one near the coflow region, which is expected since the measurement is normalized by room temperature N_2, which is the same gas

in the coflow. While the instantaneous profiles show a large flat region of minimum signal, the average profiles display a bit more of curvature and a smaller flat region of minimum signal. This is due to some radial motion of the heated jets during operation. While the post processing algorithm was effective at eliminating samples that show coflow contamination near the measurement region, it did not identify samples that exhibited an intact potential core that were simply displaced some small distance in the radial direction. The averaging effect of this small "side-to-side" movement of the jet potential core leads to the observed average FRS signal profiles exhibited in Fig. 6. However, it is noted that the average value in the analysis region (small dashed black box) is identical to that of the instantaneous samples. Thus, the average FRS signal in the analysis region, which is used to assess the results below, is not affected by small radial drifts of the jet potential core. The results shown in Fig. 6 give confidence that all reported measurements were performed in the jet potential core and thus the measured FRS signal is from a single species for all conditions tested.

2.2 Binary mixture measurements

The binary mixture measurements were performed within the same test section as the temperature–dependent single-species measurements, with the exception that a long circular tube replaced the in-line heater since the measurements were performed at room temperature. The circular tube has a smooth interior profile that facilitated fully developed pipe flow at the exit of the tube. This ensured a stable jet potential core with no "contaminated" samples. The FRS signals of four pairs of binary mixtures (containing combustion-relevant species) were examined as a function of mole fraction. Mixture pairs were chosen to test the assumption that the measured FRS signal from a mixture can be described by the mole fraction-weighted average of the FRS signals from each constituent. The mixtures can be described by a molecular weight ratio, R_{MW} and a ratio of Rayleigh scattering cross sections, R_σ. First, binary mixtures of fuels (CH_4 and H_2) with N_2 (the major component of air) were examined. For the N_2: CH_4 mixture, $R_{MW} = 1.75$ and $R_\sigma = 0.47$, while for the N_2:H_2 mixture, $R_{MW} = 14.3$ and $R_\sigma = 4.7$. Subsequently, mixtures of two fuels CH_4 and H_2 were examined, where $R_{MW} = 7.96$ and $R_\sigma = 10$. Finally to explore the difference between gases with a large difference in both molecular weight and scattering cross section, a binary mixture of CO_2 and H_2 was examined, where $R_{MW} = 21.8$ and $R_\sigma = 11.2$.

For each of the four binary mixtures, the FRS signal was measured at six specific mixture ratios spanning the complete range of possible mixtures. The mass flow rate for each gas was controlled by a user-calibrated mass flow controller (Alicat) and the target mixture ratio was set by adjusting each species' flow rates accordingly. The actual

mixing state, which accounts for small errors in flow rates, was determined in situ using the LRS measurements. The mole fraction for "component 1" is determined from the following equation:

$$X_1 = \frac{S_{\text{LRS,mix}} - S_{\text{LRS,2}}}{S_{\text{LRS,1}} - S_{\text{LRS,2}}}, \tag{7}$$

where $S_{\text{LRS,mix}}$ is the LRS signal from any mixture with $0 \le X_1 \le 1$ (and corresponding $X_2 = 1 - X_1$), $S_{\text{LRS,1}}$ is the LRS signal when the gas mixture is made up entirely of component 1, and $S_{\text{LRS,2}}$ is the LRS signal when the gas mixture is made up entirely of component 2.

2.3 Near-adiabatic "Hencken" flame measurements

A commonly used burner in combustion research is the near-adiabatic, flat-flame "Hencken" burner [39]. This burner produces a flat-flame that stabilizes above the burner surface thereby drastically reducing the heat loss from the flame to the burner surface. Since the configuration results in near-adiabatic conditions, the species and temperature within the post-flame region are known with a high degree of accuracy (as described below). The burner has three separate gas inputs for fuel, oxidizer, and an inert gas. The fuel and oxidizer streams exit the burner surface separately in a series of small nozzle arrays. The fuel and oxidizer mix and ignite above the burner surface. The small mixing region provides a buffer zone between the burner surface and flame. The inert gas (nitrogen in this case) exits in a coflowing region surrounding the main burner matrix and is used to provide a balance of momentum such that the flame is as flat as possible across the whole burner surface and not curved downwards towards the edge of the burner surface due to shear. Additionally, it provides a buffer against dust entering the camera field of view. More information about the design and operation of the burner can be found in Ref. [39].

The flow rate for each gas in the current experiment was controlled by mass flow controllers (Alicat), which were calibrated against a laminar flow element (LFE; Meriam Process Technologies) to ensure accurate equivalence ratios for the flames. FRS and LRS measurements of H_2/air and CH_4/air flames at various equivalence ratios, ϕ, were performed. For the H_2/air flames, the equivalence ratio ranged from 0.2 to 2.4, and for the CH_4/air flames, the equivalence ratio spanned from 0.7 to 1.3. For the H_2/air flames, measurements were performed at 30 mm above the burner surface, while for the CH_4/air flames, the measurements were performed at 18 mm above the burner surface. Similar to the temperature-dependent, single species measurements, the FRS and LRS signals in the post-flame region were normalized by reference measurements in pure N_2 at $T = 296$ K. Example normalized profiles from a $\phi = 0.95$ H_2/air flame
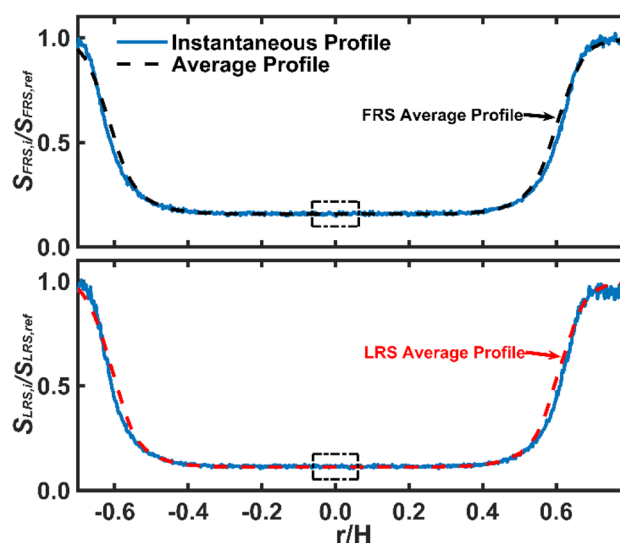
Fig. 7 Example FRS (top) and LRS (bottom) signal profiles from an H_2/air flame operating at $\phi = 0.95$ flame, stabilized above the surface of a near-adiabatic Hencken burner Measurements are normalized by reference measurements in pure nitrogen at $T = 296$ K. Single-shot (blue dashed) profiles are plotted with average profiles from FRS (black) and LRS (red) measurements. Dashed box indicates region where the FRS and LRS signal ratios are determined for analysis

are shown in Fig. 7. The single shot and average profiles shown in Fig. 7 are consistent with profiles from all other fuel and ϕ cases. The large flat region in the center of the profiles provides an unambiguous LRS and FRS signal representing the high temperature gas mixture found within the post-flame region of these flames. It is clear from the agreement between the single-shot and average profiles that the flame was stable and the measurements were performed with high signal-to-noise.

For a given ϕ, equilibrium calculations were performed using the NASA chemical equilibrium analysis program (CEA), in conjunction with the signal measurements, to determine both the gas temperature as well as the mole fractions of major species including N_2, O_2, CH_4, H_2, CO_2, H_2O, CO, and OH. The process to determine the temperature and species concentration is the same as presented in [40] to determine the coflow temperature of jet-in-hot-coflow auto-ignition experiments. First, adiabatic equilibrium is assumed and the CEA program is run to calculate the product species. Using the adiabatic flame temperature (T_{ad}) and the associated mole fractions, a synthetic LRS signal ratio is calculated and compared to the measured LRS signal ratio. In the case where the measured LRS signal ratio exceeds the theoretical signal ratio (indicating some level of heat loss), CEA was run with a temperature $T < T_{\text{ad}}$, yielding new mole fraction values (but still at an equilibrium condition for $T < T_{\text{ad}}$). This process was repeated until the measured and synthetic LRS values converged. In this way, the LRS measurements

accounted for heat loss and provided an accurate estimate of both the post-flame temperature and the species composition in the post-flame zone. The derived temperatures were within 3.5%, 2%, and 7.5% of the adiabatic equilibrium temperature for the H_2/air, lean CH_4/air, and rich CH_4/air flames, respectively. In general, the estimated mole fractions were within a few percent of the adiabatic equilibrium values. Once the temperature and species mole fractions are determined from this process, those values are used as the conditions in which to calculate a synthetic FRS signal. Comparison of the FRS measurements with a synthetic FRS signal generated using the Tenti S6 model provides an indirect method to assess both (1) the Tenti S6 RBS model at high temperatures and (2) the mixture-averaged FRS signal assumption outlined in Eq. (4). These measurements also provide an additional indirect evaluation of gas-phase H_2O, which is not assessed within the temperature-dependent, single-species measurements, yet is an important major species within combustion environments.

2.4 FRS (Tenti S6 + I_2 absorption) model for combustion species

Since our basis for evaluating the Tenti S6 model is a comparison between measured and synthetic FRS signals, a few comments on the generation of the synthetic FRS signals are warranted. The Tenti S6 model only considers Placzek trace scattering in the calculation of the Cabannes line, while measurements of scattered light will consist of three different components: (1) Placzek trace scattering, (2) Q-branch rotational Raman scattering, and (3) Stokes and anti-Stokes rotational Raman scattering. For a more complete comparison between measured and calculated FRS signals, Q-branch and S/AS Raman scattering effects are added into the synthetic signal calculations as described in Appendix 1. For a single species, Eq. (2) is modified to

$$S_{\text{FRS},i} = \text{CI}_0 n_i \psi_i', \tag{8}$$

where ψ_i' is a modified FRS specific variable which can be expressed as

$$
\begin{aligned}
\psi_i' = {} & \sigma_i^t \int_\nu \mathcal{R}_i(\nu_r) \tau_{I2}(\nu) \tau_{\text{BPF}}(\nu) \mathrm{d}\nu \\
& + \sigma_i^Q \int_\nu \mathcal{R}_i^Q(\nu_r) \tau_{I2}(\nu) \tau_{\text{BPF}}(\nu) \mathrm{d}\nu \\
& + \sum_{J=0}^\infty \sigma_i^{J \to J'} F_J \int_\nu \mathcal{R}_i^{J \to J'}(\nu_r, \Delta\nu_{J \to J'}) \tau_{I2}(\nu) \tau_{\text{BPF}}(\nu) \mathrm{d}\nu.
\end{aligned}
\tag{9}
$$

In Eq. (9), the last two terms represent the Q-branch and Stokes/anti-Stokes Raman scattering contributions to the total scattering signal, respectively. σ_i^t, σ_i^Q, and $\sigma_i^{J \to J'}$ are the Placzek trace[2], Q-branch rotational Raman, and Stokes/anti-Stokes rotational Raman scattering components of the differential Rayleigh scattering cross section, respectively; J is the initial rotational–angular momentum quantum number; F_J is the fraction of molecules in state J; $\Delta\nu_{J \to J'}$ are the rotational Raman shifts; $\mathcal{R}_i(\nu_r)$, $\mathcal{R}_i^Q(\nu_r)$, and $\mathcal{R}_i^{J \to J'}(\nu_r, \Delta\nu_{J \to J'})$ are the spectral lineshapes for the Placzek trace, Q-branch rotational Raman, and Stokes/anti-Stokes rotational Raman scattering, respectively; and $\tau_{\text{BPF}}(\nu)$ is the transmission of the bandpass filter centered around 532 nm. Details concerning the generation of the Q-branch and Stokes and anti-Stokes rotational Raman spectra is discussed in Appendix 1. As discussed below, with the exception of CO_2, the rotational Raman scattering contributions are small and thus the comparison of the measured and synthetic FRS signals is an evaluation of the Tenti S6 RBS model.

For a single species (at any temperature, T), the normalized synthetic FRS signal based on Eqs. (8) and (9) is generated by

$$
\left. \frac{S_{\text{FRS},i}(T)}{S_{\text{FRS,ref}}(T_{\text{ref}})} \right|_{\text{syn}} = \frac{T_{\text{ref}}}{T} \times \frac{\psi_i'(T)}{\psi_{\text{ref}}'(T_{\text{ref}})}, \tag{10}
$$

where $S_{\text{FRS,ref}}$ is the FRS signal calculated at a reference condition, which is pure N_2 at $T_{\text{ref}} = 296$ K. For near-adiabatic flame measurements, the normalized synthetic FRS signal from the in-flame gas mixture is generated using Eq. (4) and can be represented as

$$
\left. \frac{S_{\text{FRS,mix}}(T)}{S_{\text{FRS,ref}}(T_{\text{ref}})} \right|_{\text{syn}} = \frac{T_{\text{ref}}}{T} \times \frac{\sum_i^N X_i \psi_i}{\psi_{\text{ref}}(T_{\text{ref}})}, \tag{11}
$$

where X_i is the mole fraction of the major combustion species estimated during data analysis as described above. For the flame temperatures considered, the total rotational Raman effects were < 1% and thus were not considered in the analysis. Average wavenumbers from the experiment (as discussed below) are used to determine where the incident laser is centered relative to the spectra of the I_2 cell. The Rayleigh scattering cross sections are obtained from [41, 42] and the I_2 spectral transmission ($\tau(\nu)$) profile is determined using a code originally developed by Forkey et al. [34] that calculates the absorption spectra of the $B\left(^3\Pi_{0^+u}\right) \leftarrow X\left(^1\Sigma_g{}^+\right)$ electronic transition of iodine. The code has been modified to account for non-resonant background effects [43] and

---

[2] The trace scattering cross section, σ_i^t is calculated as $\sigma_i - \left(4\rho_i/3 - 4\rho_i\right)$, where ρ_i is the depolarization ratio of species i.

has been validated experimentally to a certain extent [34, 44, 45]. To evaluate the Tenti S6 model, the calculated I_2 absorption spectrum is treated as accurate.

As described above, the S6 kinetic model from Tenti et al. [5] is based on solving a linearized Boltzmann equation, where the intermolecular collisions are treated semiclassically. In the current work, N_2, O_2, H_2, CH_4, Ar, CO_2, H_2O, CO, and OH are considered. To calculate the scattering profiles of each species, values for shear viscosity (μ), thermal conductivity (κ), bulk viscosity (μ_B), and the internal specific heat capacity per molecule (c_{int}) are needed as inputs. Table 2 in Appendix 2 tabulates the values of μ_B, and c_{int} used in the current study. The shear viscosity, μ, and the thermal conductivity, κ, are independent of pressure, but are dependent on temperature. When possible, the temperature-dependent values of μ and κ are determined from the NIST database [46]. The temperature-dependent values are tabulated to form a lookup table that is accessed for any temperature within the specified range via interpolation. For higher temperatures beyond what is available within the NIST database, the NASA polynomial fits [47] are used for μ and κ.

The internal specific heat capacity (c_{int}) and the bulk viscosity (μ_B) are related to the relaxation of the internal degrees of freedom of a gas species. Monatomic gases are free of rotational or vibrational energy and thus $c_{int} = \mu_B = 0$. However, for molecular gases, rotational and vibrational modes may be active and couple to the molecule's center-of-mass momentum. The values of c_{int} depend on the number of internal degrees of freedom that are accessible, which depends on the relative frequencies of the density fluctuations and relaxation rates of the internal degrees of freedom as described in Appendix 2. For molecular gases with no active (or accessible) vibrational degrees of freedom, $c_{int} = 1$ and 3/2 for linear and non-linear molecules, respectively. If the vibrational modes couple to the molecule's center-of-mass momentum, then c_{int} increases. For diatomic molecules, vibrational relaxation is very slow and thus vibrational motion is ignored and $c_{int} = 1$. In addition, Pan et al. [48] showed that for coherent RBS measurements of CO_2 at optical frequencies, the vibrational modes are frozen (on the timescale of light scattering experiments) and the molecule is properly treated as having $c_{int} \approx 1$. In the current work, the vibrational modes are assumed to be frozen for both CO_2 and CH_4 ($c_{int} = 1$ and 3/2, respectively) due to the slower vibrational relaxation times ($\tau_v > 1 \times 10^{-6}$ s at $P = 1$ atm) [49] as compared to the typical period of sound ($O(10^{-9}$ s)) for light scattering experiments. For H_2O, both the rotational and vibrational modes are assumed to be active due to its much faster vibrational relaxation time ($10^{-10} < \tau_v < 10^{-8}$ s at $P = 1$ atm and $3000 > T$ (K) > 300 K) (e.g., [50, 51]) and thus, $c_{int} > 3/2$ and allowed to vary as a function of temperature. In Appendix 2, the temperature-dependent value of c_{int} for H_2O is derived and the sensitivity of H_2O FRS signals to

variations in c_{int} is assessed. It is found that while there are some changes to the calculated RBS spectra at low temperatures, there is an overall negligible effect on the calculated synthetic FRS signal.

For molecular species, the value of μ_B depends on the number of internal degrees of freedom (rotational and vibrational) that contribute to the bulk viscosity. Values for μ_B are not well known for the majority of species considered in combustion environments, especially at elevated temperatures. In addition, the majority of reported values of μ_B are derived from ultrasound experiments at MHz frequencies. Since light scattering experiments are characterized with sound frequencies on the order of 1 GHz, the validity of μ_B values measured at lower frequencies is unknown, especially for polyatomic molecules. For example, several research groups have found that the value of μ_B for CO_2 is approximately 1000 times smaller than values measured in acoustical experiments at MHz frequencies [12, 48, 52, 53]. Recently, high-resolution spontaneous and coherent RBS measurements have yielded values of μ_B directly from the measured spectra of N_2, O_2, CO_2, CH_4, and other gases at low temperatures [12–14, 53] as first suggested by Pan et al. [48]. In addition, Gu and Ubachs [13] have determined the temperature dependence of μ_B for N_2, O_2, and air over a small temperature range of 250–340 K. They found that μ_b increased linearly with temperature, although it is unknown whether this trend continues for higher temperatures or for other species. Cramer [54] provides temperature-dependent numerical estimates of the bulk viscosity for a number of well-known ideal gases including N_2, H_2, CO, CH_4, H_2O, and CO_2, which are considered in this study. At room temperature conditions, the results for diatomic species generally agree with many of the published values available within the literature. However, for polyatomic molecules, the numerical estimates were made assuming that the vibrational modes contribute to the value of μ_B, which yield values of μ_B that may be several orders of magnitude too high when the vibrational modes are frozen as is the case of CH_4 and CO_2 with light scattering experiments. In addition, many of the temperature ranges provided in [54] are quite limited and do not provide a general relationship for the full temperature range of interest for combustion species. In this manner, we develop temperature-dependent expressions for the bulk viscosity for each species based on available rotational and vibrational relaxation times found within the literature. Rationale for the selected values of μ_B for each species is given in Appendix 2 as well as assessment of the sensitivity of variations in μ_B on the calculated synthetic FRS signals. Overall, the results show that for reasonable variations from our selected values of μ_B, including the temperature dependence, there is a minimal sensitivity of the synthetic FRS signals to μ_B, assuming that the bulk viscosity does not approach zero.

Table 1 Measured LRS and FRS signal ratios at $T = 296$ K compared to published values of Rayleigh scattering cross sections and calculated synthetic FRS signals, respectively

Gas	$\left.\dfrac{S_{\text{LRS},i}}{S_{\text{LRS},N_2}}\right|_{\text{exp}}$	σ_i/σ_{N_2} [41]	$\left.\dfrac{S_{\text{FRS},i}}{S_{\text{FRS,ref}}}\right|_{\text{exp}}$	$\left.\dfrac{S_{(\text{FRS}),i}}{S_{(\text{FRS}),\text{ref}}}\right|_{\text{syn}}$
Ar	0.866	0.865	0.649	0.647 (0.650)
Air	0.970	0.969	0.962	0.979 (0.972)
H_2	0.216	0.213	0.325	0.318 (0.315)
CO_2	2.394	2.390	1.881	1.888 (1.687)
CH_4	2.188	2.140	2.929	2.801 (2.799)
CO	1.254	1.250	1.258	1.252 (1.249)

The synthetic FRS signals are calculated at the same wavenumber as the measurements. The values shown in () represent the synthetic signal ratio calculated without estimating rotational Raman scattering contributions

3 Results and discussion

The FRS signal measurements are first processed using the wavenumber filtering technique as described in Ref. [22]. That is, instantaneous measurements that have a wavenumber fluctuation of greater than ±0.001 cm^{-1} from the mean wavenumber (ν) are removed and not considered in the results. In this manner, wavenumber (wavelength) variations do not have to be considered in the interpretation of the results. The average wavenumber values are then used to determine the relative spectral position between the RBS lineshapes and the I_2 transmission spectra for the calculation of the synthetic FRS signal ratios that are compared with the measured FRS signal ratios.

3.1 Temperature-dependent FRS signals for single species

As a first assessment of the measurements, the relative LRS signal ratio of each gas, $S_{\text{LRS},i}/S_{\text{LRS},N2}$ at $T = 296$ K is compared to known relative Rayleigh scattering cross-section, σ_i/σ_{N2} [41] as shown in Table 1. The measurements for each gas species agree very well with published scattering cross sections [41], with a maximum difference of < 2.2%, which is less than the uncertainty in the Rayleigh scattering cross section measurements. These results provide a high degree of confidence in the LRS measurement technique (which will be used to determine the gas-phase temperature) and in the ability to provide a reliable uncontaminated FRS/LRS signal from the species of interest in the heated jet configuration.

The measured relative FRS signals, $S_{\text{FRS},i}(T)/S_{\text{FRS,ref}}$ for each individual gas species are compared to synthetic FRS signals calculated using Eq. (10). Table 1 shows the results of $S_{\text{FRS},i}/S_{\text{FRS,ref}}$ at $T = 296$ K and $P = 1$ atm. Comparisons between the measured FRS signal ratios and the synthetic
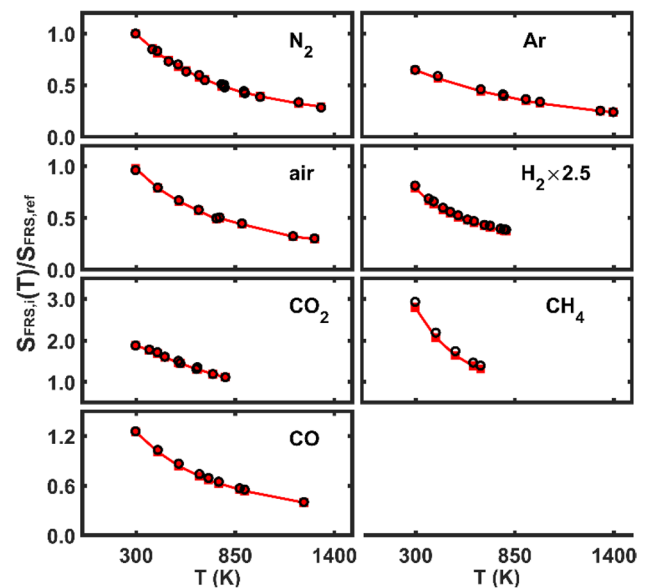
Fig. 8 Temperature-dependent FRS signals for various gases. All FRS signal ratios are normalized by results from pure N_2 at 296 K. Experimental (black circles) and synthetic (red squares) results are shown for N_2, Ar, air, H_2, CO_2, CH_4, and CO. Note the signal ratio for H_2 has been multiplied by 2.5 for easier observation

FRS signal ratios show excellent agreement with < 2% error between the measurements and the synthetic signal ratios for Ar, air, H_2, CO_2, and CO and 4% error for CH_4. It is noted that the inclusion of the Q-branch and Stokes/anti-Stokes rotational Raman scattering contributions in the synthetic signals have negligible effects on the results with the exception of CO_2. For N_2, O_2, CO, and H_2, the estimated combined contribution of the Q-branch, Stokes, and anti-Stokes rotational Raman scattering to the total scattering signal is < 2.5% at 296 K and decreases with increasing temperature (see Appendix 1). In this manner, the accuracy of the synthetic FRS signals implies accurate RBS lineshape predictions at 296 K using the Tenti S6 model. For CO_2, rotational Raman scattering is approximately 16% of the total scattering signal at 296 K. As shown in Table 1, the exclusion of rotational Raman scattering leads to a discrepancy of approximately 10.3% between the measured and synthetic FRS signals. When including rotational Raman effects, the measured and synthetic CO_2 FRS signals are within 0.3% of one another. This likely implies that the Placek-trace portion of the RBS lineshape is accurately predicted using the Tenti S6 model, which would be consistent with the reasonable agreements observed between measured and modeled CO_2 RBS spectra presented by Gu and Ubachs [13]. In their work, there are small, but noticeable differences between measured and modeled spectra near the center frequency that may be due to the exclusion of Q-branch rotational Raman scattering contributions (~4%).

Figure 8 shows the measured and calculated synthetic FRS signal ratios as a function of temperature for seven gaseous species. The black circles are the direct measurements of the temperature-dependent FRS signal ratios of the various gases referenced to N_2 at 296 K. The experimental results represent the average of approximately 350 samples per data point. The red squares are the synthetic FRS signal ratios calculated using Eq. (10) in conjunction with the Tenti S6 model, the Forkey I_2 model, and additional rotational Raman scattering calculations (Appendix 1) as described above and at the temperature and average wavenumber measured during the experiment. For each data point presented, the uncertainty due to shot noise is less than the region occupied by the reported symbol, and thus, the symbol size can be taken as an uncertainty estimate.

It is observed in Fig. 8 that the synthetic and measured FRS signal ratios demonstrate good agreement overall. The N_2, Ar, air, CO, and CO_2 results show excellent agreement over the full temperature range of 296–1400 K, where the largest discrepancy is < 5%. While not shown here, the exclusion of rotational Raman scattering contributions for CO_2 led to notable discrepancies between the synthetic and experimental results for lower temperatures (< 600 K). However, as temperature increases the difference between the synthetic results and measurements reduces as expected based on the results shown in Fig. 12 (Appendix 1) which shows that the contribution of the rotational Raman scattering signal to the total signal decreases with increasing temperature. Since the formation of CO_2 only becomes important at elevated temperatures and peak CO_2 mole fractions are typically less than 0.15 under combustion conditions, it is expected that the total contribution of rotational Raman scattering will be less than 1.5% of the total FRS signal. Thus, the exclusion of rotational Raman scattering contributions is not a major concern for the accuracy of the FRS thermometry techniques used in reacting flows.

In terms of the fuels, both H_2 and CH_4 show good agreement between the modeled results and measurements throughout the range of temperatures tested. Higher temperatures were not achieved for the fuels due to limitations of the heaters. However, this should not be a significant issue since the contribution from fuels to the total FRS signal in the majority of reacting flows will be small at higher temperatures due to reaction. Since the fuels will be consumed at lower temperatures, the assessment of the accuracy of the RBS spectral modeling only is critical at lower temperatures. A significant finding from this work is that the synthetic FRS signals and hence the predicted RBS lineshapes computed using the S6 model are sufficiently accurate over a broad range of temperatures considered for several combustion-related species.
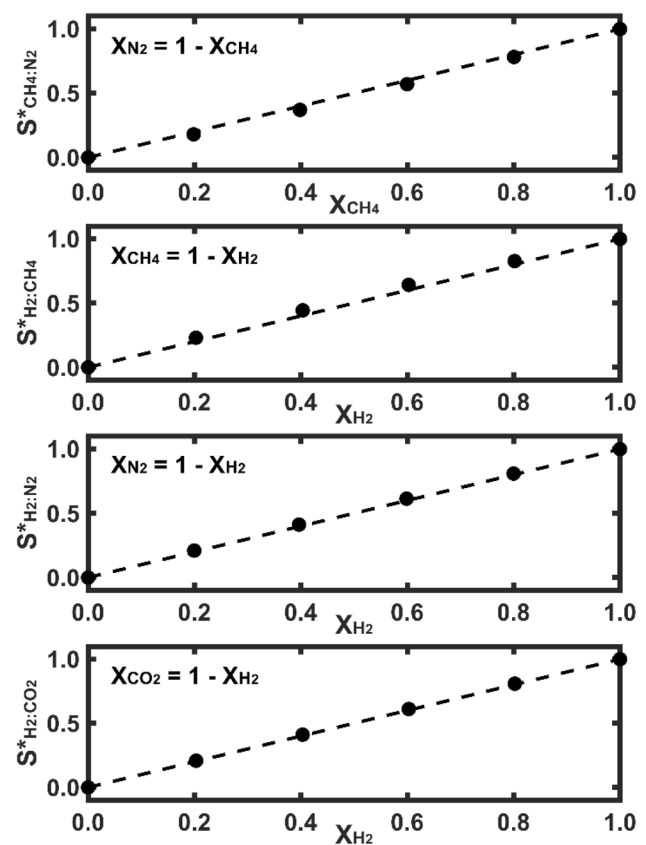

Fig. 9 Normalized FRS signal versus mole fraction for various binary gas mixtures at room temperature and pressure. Experimental results are shown as black symbols. The dashed, black line represents the ideal linear behavior

3.2 Binary gas mixtures

To test the assumption that the FRS signal from a gas mixture in the kinetic regime can be treated as the mole fraction-weighted average of the FRS signal from each component, FRS measurements were conducted in binary mixtures at atmospheric pressure and temperature. For a binary mixture, validation of this assumption implies that the relationship between the FRS signal and the mole fraction of one of the components is linear. In this manner, a normalized FRS signal is defined as

$$S_{1:2}^*(X_1) = \frac{S_{\text{FRS,mix}} - S_{\text{FRS,2}}}{S_{\text{FRS,1}} - S_{\text{FRS,2}}} , \qquad (12)$$

where X_1 is the mole fraction of component 1 (with a corresponding mole fraction of component 2 given by $X_2 = 1 - X_1$), $S_{\text{FRS,mix}}$ is the FRS signal from a mixture of components 1 and 2, $S_{\text{FRS,1}}$ is the FRS signal from a gas consisting of component 1 only and $S_{\text{FRS,2}}$ is the FRS signal from a gas consisting of component 2 only. It is noted that

$S^*_{1:2}$ is bound between 0 and 1, when X_1 is varied between 0 and 1.

Shown in Fig. 9 are plots of the normalized FRS signal $S^*_{1:2}$ as a function of mole fraction of the mixture components (only the mole fraction value on one component is shown, but the other is determined via the expression in the insert). The results represent the average of approximately 550 samples per data point. As in Fig. 8, the uncertainty of each measurement can be considered as the size of the symbols. For each of the four mixtures, the measured normalized FRS signal, $S^*_{1:2}$ (shown as solid symbols), closely follows the ideal linear curve (shown as a solid black line). Least-squares linear fits applied to the data yield an R squared value of > 0.997 for all four binary mixtures indicating a high degree of linearity for the measured response curves. These results imply that for the current set of conditions, the assumption that total FRS signal can be represented as the mole fraction-weighted average of the components of the mixtures is valid. If the mole fraction-weighted assumption is valid for atmospheric temperature and pressure conditions ($y \approx 1$), then it is expected to hold for higher temperature (lower densities; decreasing y) conditions in combustion environments at atmospheric pressure or more generally, conditions that can be characterized as being in the 'kinetic' regime.

3.3 Near-adiabatic flame results

Simultaneous FRS and LRS measurements were made within the post-flame region of near-adiabatic flames produced by the Hencken burner as described above. A full range of equivalence ratios of H_2/Air ($0.2 < \phi < 2.4$) and CH_4/Air ($0.7 < \phi < 1.3$) were tested, which results in a large range of temperatures and species compositions. Figure 10 shows the comparison between the measured FRS signals and the synthetic FRS signals calculated using measured temperatures, estimated species mole fractions (see above), and the combination of I_2 absorption and Tenti S6 RBS models (see Eq. 9). Figure 10a shows the results from the set of CH_4/air flames and Fig. 10b shows the results from the set of H_2/air flames. For both sets of the flames, the measured FRS signals are represented by the black, circular symbols and the synthetic FRS signals are represented by the red, square symbols. The experimental results represent the average of 250 to 300 samples per data point and the uncertainty of each measurement can be taken as the size of the symbols.

The results show that there is an excellent agreement between measured and synthetic FRS signals for both the CH_4/air and H_2/air flames across the wide range of equivalence ratios examined. This can be seen clearly in Fig. 10c, which plots the measured FRS signals as a function of the synthetic FRS signals for all CH_4/air and H_2/air flame cases. For the CH_4/air flames, there is less than 1.2% difference
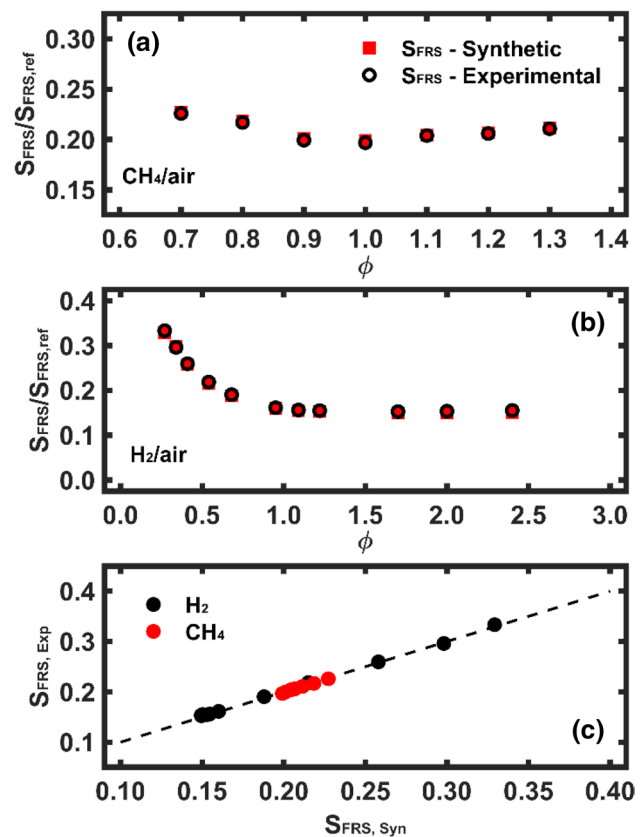
Fig. 10 a Normalized FRS signal versus equivalence ratio for a CH_4/air Hencken flame. Experimental results are shown as black symbols and estimated synthetic results are shown as red squares. **b** Normalized FRS signal versus equivalence ratio for a H_2/air Hencken flame. Experimental results are shown as black circles and estimated synthetic results are shown as red squares. **c** Comparison of experimental normalized FRS signal versus synthetic normalized FRS signal for both the CH_4/air (red circles) and H_2/air (black circles) Hencken flames

between the measured and synthetic FRS signals, while there is less than 2% difference between measured and synthetic FRS signals for the H_2/air flames for $0.2 < \phi < 1.7$. For $\varphi = 2.0$ and 2.4, the difference between measured and synthetic FRS signals is $\sim 3\%$. The current results are consistent with results from Kearney et al. [55] who compared FRS-derived temperature measurements with those obtained from CARS thermometry in a series of CH_4/air flames stabilized above the surface of a Hencken burner. The FRS measurements were converted to temperature assuming adiabatic equilibrium for the species concentrations and the use of the Tenti S6 model. Their results showed good agreement between the FRS and CARS temperature measurements for $\varphi < 1.3$ suggesting sufficient accuracy in the S6 model.

In the current work, the agreement between measured and synthetic FRS signals over the broad range of equivalence ratios is notable since (1) the calculation of the synthetic FRS signal assumes the mixture-weighted formulation

shown in Eqs. (4) and [8] and (2) the various species mole fractions change considerably over the full range of equivalence ratios considered. For example, for the H_2/air flames, $0 \leq X_{H2} \leq 0.33$; $0.44 \leq X_{N2} \leq 0.75$; $0\ X_{O2} \leq 0.15$; and $0.11 \leq X_{H2O} \leq 0.33$ for $0.2 \leq \phi \leq 2.4$; while for the CH_4/air flames, $0.66 \leq X_{N2} \leq 0.74$; $0 \leq X_{O2} \leq 0.06$; $0.14 \leq X_{H2O} \leq 0.19$; $0 \leq X_{CO} \leq 0.06$; $0.05 \leq X_{CO2} \leq 0.09$ for $0.7 \leq \phi \leq 1.3$. From the good agreement between the measured and synthetic FRS signals, it is inferred that the assumed mixture-weighted formulation of Eq. (4) is justified within the kinetic regime, further corroborating the results of the binary mixture results shown above. Also, it can be inferred that the RBS spectra of the relevant combustion species are calculated accurately, at least over the range of temperatures represented by the current atmospheric pressure flame conditions.

4 Summary and conclusions

The goal of this work was to test the Tenti S6 Rayleigh–Brillouin scattering (RBS) model [5] for combustion-relevant species over a broad range of temperatures with relevance towards filtered Rayleigh scattering (FRS) thermometry measurements in flames. Testing of the Tenti S6 model was performed by comparing measured FRS signals to synthetic signals generated from the combination of the Tenti S6 RBS model and an experimentally verified I_2 transmission model. To calculate the RBS profiles for any species, values for shear viscosity (μ), thermal conductivity (κ), bulk viscosity (μ_B), and the internal specific heat capacity per molecule (c_{int}) are needed as inputs to the Tenti S6 model. The sensitivity of the calculated synthetic FRS signals to variations in the bulk viscosity and internal specific heat capacity (for polyatomic molecules) was examined. The results showed that for reasonable variations in μ_B and c_{int}, that even exceeded the uncertainty of the values specified in the model, there were minimal effects on the calculated synthetic FRS signal.

Assessment of the Tenti S6 model was performed over a broad range of operating conditions, which included several gas-phase species, gas mixtures, and temperatures. First, simultaneous laser Rayleigh scattering (LRS) and FRS measurements were performed for several combustion-relevant gases (N_2, Ar, air, CH_4, CO_2, H_2, and CO) as a function of temperature. The LRS measurements were used to determine the in situ temperature and the measured and synthetic FRS signals were compared across a wide temperature range (296–1400 K). Excellent agreement ($<4\%$ difference) was observed between the measured and synthetic FRS signals for all species across all temperatures examined. For CO_2, inclusion of Q-branch, Stokes, and anti-Stokes rotational Raman scattering contributions was necessary to achieve agreement between the measurements and synthetic FRS

signals of pure CO_2. The rotational Raman scattering contribution to the total measured FRS signal decreases with increasing temperature, which is important for FRS measurements in reacting flows as CO_2 is formed only at higher temperatures. This combined with the fact that peak CO_2 mole fractions do not exceed 0.10–0.15 in hydrocarbon/air combustion systems implies that the inclusion of rotational Raman scattering effects is not necessary for accurate thermometry via FRS. Overall, the temperature-dependent FRS measurements provided confidence in the accuracy of the Tenti S6 RBS model for single species at low, moderate, and elevated temperatures.

Second, simultaneous FRS and LRS measurements were made within a series of two-component mixtures of CH_4/N_2, H_2/N_2, CH_4/H_2, and CO_2/H_2 to examine the FRS signal dependence as a function of mixture composition. Specifically, the mixture pairs and subsequent measurements were performed to test the assumption that the measured FRS signal from a mixture can be described by the mole fraction-weighted average of the FRS signals from each constituent when the scattering process falls within the 'kinetic' regime. Mixtures with a wide range of molecular weight ratios ($1.75 \leq R_{MW} \leq 21.8$) and ratios of Rayleigh scattering cross sections ($0.47 \leq R_{MW} \leq 11.2$) were examined, while the LRS measurements were used to provide accurate measurements of mole fraction for each component of the mixtures. For all mixtures, the measured FRS signal was linear with mole fraction of either component, implying that for the current test cases ($y = O(1)$), the assumption that total FRS signal can be represented as the mole fraction-weighted average of the components of the mixtures is valid [see Eq. (4)].

Finally, simultaneous FRS and LRS measurements were performed within the post-flame region of near-adiabatic H_2/air ($0.2 < \phi < 2.4$) and CH_4/air ($0.7 < \phi < 1.3$) flames stabilized above the surface of a Hencken burner. The measured FRS signals were compared to synthetic FRS signals calculated at the temperatures and species composition estimated from the LRS measurements. Excellent agreement was observed between the measured and synthetic FRS signal ratios for both flame systems across all equivalence ratios examined. Overall these results indicate that the Tenti S6 RBS model predicts the RBS spectra of combustion-relevant gas species at combustion-relevant gas temperatures with sufficient accuracy. Furthermore, the Tenti S6 model, in conjunction with the I_2 model developed by Forkey et al. [34], should be sufficient for facilitating quantitative FRS-based measurements in reacting flows.

The in-flame results, combined with the binary mixing results also indicate a more general result; that is, for conditions characterized as being in the 'kinetic regime', the FRS signal from a mixture can be described as the mole fraction-weighted average from all constituents, as previously assumed in previous works, but not verified.

Appendix 1: calculation of rotational Raman scattering spectra and FRS signal contributions

If molecules are free to rotate, "Rayleigh scattering" consists of rotational Raman scattering as well as the Placzek trace scattering. Rotational Raman scattering comprised of an un-shifted Q-branch in addition to spectrally shifted Stokes and anti-Stokes branches. The Q-branch corresponds to no change of the rotational state ($\Delta J = 0$), while the Stokes and anti-Stokes branches follow selection rules of $\Delta J = \pm 2$. The $J \rightarrow J+2$ transitions are the Stokes lines, while the $J \rightarrow J-2$ transitions are the anti-Stokes lines. The Raman shifts for the Stokes and anti-Stokes lines can be approximated as

$$\Delta\nu_{J \rightarrow J'} = -\left(4B_o - 6D_o\right)(J + 3/2) + 8D_o(J + 3/2)^3, \quad (13)$$

and

$$\Delta\nu_{J \rightarrow J'} = \left(4B_o - 6D_o\right)(J - 1/2) - 8D_o(J - 1/2)^3, \quad (14)$$

respectively, where B_o is the rotational constant for the lowest vibrational level and D_o is the centrifugal distortion coefficient.

The intensity of a single Stokes or anti-Stokes-shifted rotational Raman scattering line is given by

$$I_{J \rightarrow J'} = CI_o n_i F_J \sigma_i^{J \rightarrow J'}. \quad (15)$$

If the gas is in thermal equilibrium at temperature T, the fraction of molecules in state J can be expressed as

$$F_J = g_J(2J + 1)\exp\left(-\frac{E_J}{k_B T}\right)/Q, \quad (16)$$

where g_J is a nuclear degeneracy factor (dependent on nuclear spin), E_J is the rotational energy, and Q is the rotational partition function, determined by the normalization satisfying $\sum_{J=0}^{\infty} F_J = 1$. The rotational energy can be accurately approximated by

$$E_J = hc[B_o J(J + 1) - D_o J^2(J + 1)^2], \quad (17)$$

where h is Planck's constant. Finally, the differential rotational Raman scattering cross section, $\sigma_i^{J \rightarrow J'}$ is expressed as

$$\sigma_i^{J \rightarrow J'} = \frac{64\pi^4}{45}b_{J \rightarrow J'}\left(\nu_o - \Delta\nu_{J \rightarrow J'}\right)^4 \gamma^2, \quad (18)$$

where $b_{J \rightarrow J'}$ is a Placzek–Teller coefficient and γ is the anisotropy of the molecular polarizability tensor. The Placzek–Teller coefficients for the Stokes and anti-Stokes lines are

$$b_{J \rightarrow J+2} = \frac{3(J + 1)(J + 2)}{2(2J + 1)(2J - 3)}, \quad (19)$$

and

$$b_{J \rightarrow J-2} = \frac{3J(J - 1)}{2(2J + 1)(2J - 1)}, \quad (20)$$

respectively.

For each rotational line, Doppler and collisional broadening mechanisms lead to an intensity distribution described by a Voigt profile, which is the convolution of Gaussian (G) and Lorentzian (L) profiles. For the current work, the Voigt profile is approximated using a pseudo-Voigt profile [56]

$$V_p^{J \rightarrow J'}\left(\nu_r, \Delta\nu_{J \rightarrow J'}, \Delta\nu_T\right)$$
$$= \eta L(\nu_r, \Delta\nu_{J \rightarrow J'}, \Delta\nu_T) + (1 - \eta)G(\nu_r, \Delta\nu J \rightarrow J'), \Delta\nu_T), \quad (21)$$

where the Gaussian and Lorentzian profiles are calculated as

$$G\left(\nu_r, \Delta\nu_{J \rightarrow J'}, \Delta\nu_T\right)$$
$$= \frac{2\sqrt{\ln(2)}}{\Delta\nu_T\sqrt{\pi}}\exp\left[-4\sqrt{\ln(2)}\frac{(\nu_r - \Delta\nu_{J \rightarrow J'})^2}{\Delta\nu_T^2}\right], \quad (22)$$

and

$$L\left(\nu_r, \Delta\nu_{J \rightarrow J'}, \Delta\nu_T\right) = \frac{\Delta\nu_T}{2\pi}\frac{1}{\left(\nu_r - \Delta\nu_{J \rightarrow J'}\right)^2 + \left(\Delta\nu_T/2\right)^2}, \quad (23)$$

and η is a function of the total full width at half maximum (FWHM) parameter, $\Delta\nu_T$. An accurate formula for η is [57]

$$\eta = 1.36603\left(\Delta\nu_L/\Delta\nu_T\right) - 0.47719\left(\Delta\nu_L/\Delta\nu_T\right)^2 + 0.11116\left(\Delta\nu_L/\Delta\nu_T\right)^3, \quad (24)$$

where $\Delta\nu_L$ is the Lorentzian FWHM parameter (due to collisional broadening) and the total FWHM parameter is given by

$$\Delta\nu_T = \left[\Delta\nu_D^5 + 2.69269\Delta\nu_D^4\Delta\nu_L + 2.42843\Delta\nu_D^3\Delta\nu_L^2 + 4.47163\Delta\nu_D^2\Delta\nu_L^3 + 0.07842\Delta\nu_D\Delta\nu_L^4 + \Delta\nu_L^5\right], \quad (25)$$

where $\Delta\nu_D$ is the Gaussian FWHM parameter (due to thermal broadening). The appropriate expressions for the FWHM of the Doppler (Gaussian) and collisional (Lorentzian) broadening profiles are

$$\Delta\nu_D = 7.16 \times 10^{-6}\sqrt{\frac{T}{M_w}\frac{(2\nu_o^2 + 2\nu_o\Delta\nu_{J \rightarrow J'})}{2} + \left(\Delta\nu_{J \rightarrow J'}^2\right)^2}, \quad (26)$$

and

$$\Delta \nu_{L} = P \sqrt{\frac{T_{\text{ref}}}{T}} (AJ + B), \tag{27}$$

where P is the pressure in atmospheres, T_{ref} is a reference temperature which is 300 K in the current work, and A and B are the empirical constants describing the rotational level-dependent collisional broadening. Both the Gaussian and Lorentzian profiles (Eqs. 22 and 23) are normalized such that

$$\int_{\nu} G(\nu, \Delta \nu_{T}) = \int_{\nu} L(\nu, \Delta \nu_{T}) = 1. \tag{28}$$

Using the above expressions, the spectral lineshape for each individual Stokes and anti-Stokes rotational line is defined as

$$\mathcal{R}_{i}^{J \to J'}(\nu_{r}, \Delta \nu_{J \to J'}) = V_{p}^{J \to J'}, \tag{29}$$

and a complete Stokes/anti-Stokes spectrum for species i is generated by summing each individual rotational line as

$$S_{S/AS}(\nu) = \sum_{J=0}^{\infty} F_{J} \sigma_{i}^{J \to J'} \mathcal{R}_{i}^{J \to J'}(\nu_{r}, \Delta \nu_{J \to J'}). \tag{30}$$

Using the results of Kattawar et al. [58] and Miles et al. [16], the relative magnitude of the intensity (differential scattering cross section) of the Q-branch to the S/AS components of the rotational Raman scattering is 1/3 or

$$I_{Q} = CI_{o} n_{i} \sigma_{i}^{Q} = \sum_{J=0}^{\infty} I_{J \to J'}/3 = \frac{C}{3} I_{o} n_{i} \sum_{J=0}^{\infty} F_{J} \sigma_{i}^{J \to J'}. \tag{31}$$

The lineshape of the Q-branch is described by a Voigt profile just as the Stokes and anti-Stokes lines and the same procedure outlined above using Eqs. (21)–(29) is followed with the exception that $\Delta \nu_{J \to J'} = 0$ for the Q-branch:

$$V_{p}^{Q}(\nu_{r}, \Delta \nu_{T}) = \eta L(\nu_{r}, \nu_{T}) + (1 - \eta) G(\nu_{r}, \Delta \nu_{T}), \tag{32}$$

$$G(\nu_{r}, \Delta \nu_{T}) = \frac{2 \sqrt{\ln(2)}}{\Delta \nu_{T} \sqrt{\pi}} \exp \left[-4 \sqrt{\ln(2)} \frac{(\nu_{r})^{2}}{\Delta \nu_{T}^{2}} \right], \tag{33}$$

$$L(\nu_{r}, \Delta \nu_{T}) = \frac{\Delta \nu_{T}}{2 \pi} \frac{1}{(\nu_{r})^{2} + (\Delta \nu_{T}/2)^{2}}, \tag{34}$$

$$\Delta \nu_{D} = 7.16 \times 10^{-6} \nu_{o} \sqrt{\frac{T}{M_{w}}}, \tag{35}$$

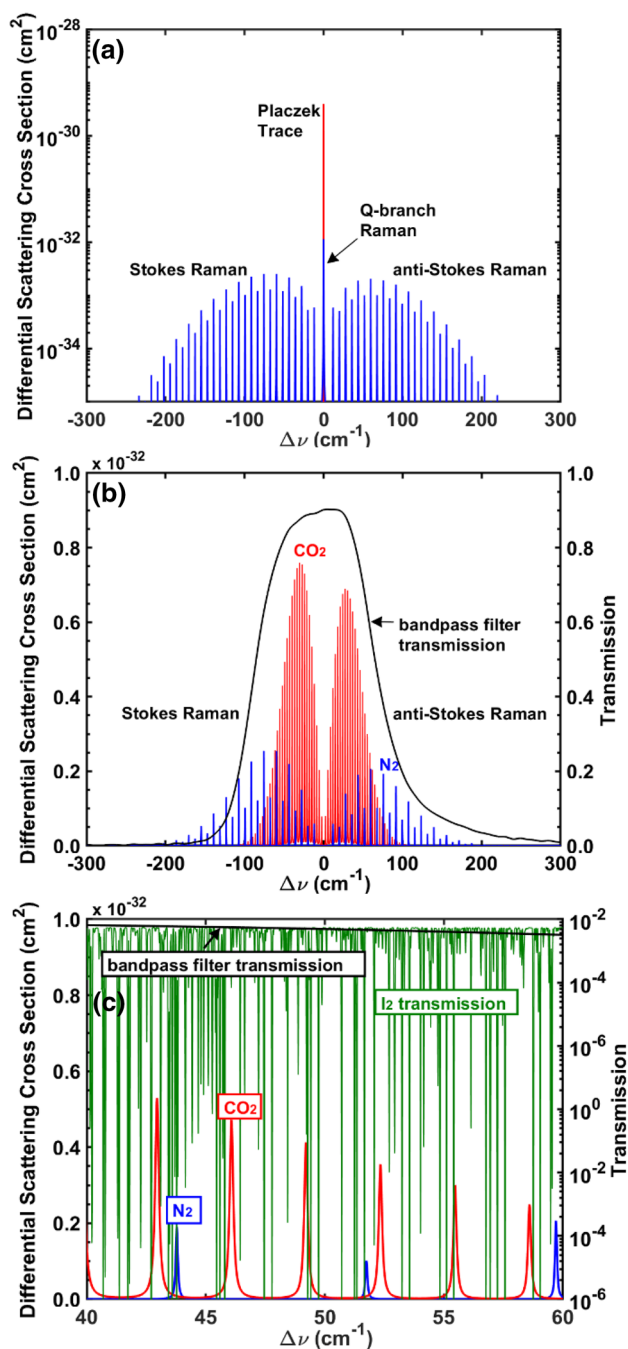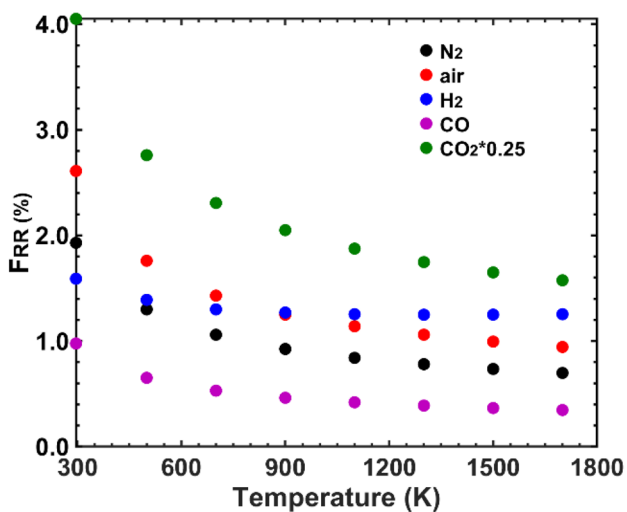$$\Delta \nu_{L} = p \sqrt{\frac{T_{\text{ref}}}{T}} B, \tag{36}$$

Fig. 11 a Calculated light scattering spectrum for N_2 at $T=296$ K and $P=1$ atm. **b** Comparison of Stokes and anti-Stokes rotational Raman scattering for N_2 ad CO_2 at $T=296$ K and $P=1$ atm. **c** "Zoomed in" region of the spectra from **b** showing the interaction between the rotational Raman lines and the I_2 filter spectrum. For S/AS rotational Raman scattering, the differential scattering cross section is plotted as $F_J \sigma_i^{J \to J'}$

Fig. 12 Variations in calculated fraction percent (FRR) of total FRS signal due to rotational Raman scattering (Q-branch and Stokes/anti-Stokes) as a function of temperature

$$\mathcal{R}_i^Q(\nu_r) = V_p^Q. \tag{37}$$

The values used for B_o, D_o, g_J, γ^2, A, and B are taken from the literature [58–63] and extrapolated to 532 nm where necessary.

Figure 11a shows an example of a calculated light scattering spectrum for N_2 at $T = 296$ K and $P = 1$ atm that compares the relative intensity of each of the components: (1) Placzek track, (2) Q-branch rotational Raman, and (3) stokes and anti-Stokes rotational Raman scattering. Integrating the various components over frequency, rotational Raman scattering comprises approximately 1.4% (0.35% Q-branch; 1.05% S/AS) of the total signal. For the majority of the species considered, the contribution of the rotational Raman scattering signal to the total scattering signal is very small as in the case of N_2 and can be neglected. However, CO_2 is an exception with the rotational Raman scattering comprising more than 6% of the total scattering signal. Figure 11b shows a comparison of the Stokes and anti-Stokes spectra for CO_2 and N_2. The total differential Raman scattering cross section of CO_2 is approximately ten times larger than that of N_2, while the total differential Rayleigh scattering cross section only is 2.39 times larger.

For the current FRS experiment, there are two more considerations to take into account: (1) the overlap of the rotational Raman scattering spectra with the 532-nm bandpass filter (BPF) and (2) the overlap of the rotational Raman scattering spectra with the I_2 absorption spectra. Both of these factors will alter the fraction of the rotational Raman scattering component that is collected within the total FRS signal. Figure 11b shows the measured spectral distribution of the BPF transmission around the center laser frequency

($\Delta \nu = 0$). It is clear that the transmission of the BPF changes significantly over the span of the rotational Raman spectra, where species such as CO_2 that have small rotational constants (and smaller spacing between adjacent rotational lines) have a higher fraction of their total signal transmitted through the BPF.

For FRS experiments, the interaction between the Rayleigh–Brillouin and I_2 spectra is well established, but because of the large spectral bandwidth of I_2, there will be overlap between the rotational Raman lines and the I_2 spectra. Figure 11c shows a "zoomed in" portion the rotational Raman spectra shown in Fig. 11b along with an overlay of a portion of the $B(^3_0\Pi_{0^+u}) \leftarrow X(^1_0\Sigma_g^+)$ electronic transition of iodine calculated with the code of Forkey et al. [34]. Figure 11c shows that the I_2 spectrum is quite dense and that many of the I_2 lines overlap with individual rotational Raman transitions. Considering the effects of the bandpass and I_2 filters, the total rotational Raman scattering signal transmitted to the detector can be written as

$$S_{RR,i} = CI_0 n_i \left[\sigma_i^Q \int_\nu \mathcal{R}_i^Q(\nu_r) \tau_{I2}(\nu) \tau_{BPF}(\nu) d\nu \right.$$
$$\left. + \sum_{J=0}^\infty \sigma_i^{J \to J'} F_J \int_\nu \mathcal{R}_i^{J \to J'}(\nu_r, \Delta\nu_{J \to J'}) \tau_{I2}(\nu) \tau_{BPF}(\nu) d\nu \right], \tag{38}$$

where $\tau_{I2}(\nu)$ and $\tau_{BPF}(\nu)$ is the transmission of the I_2 cell and bandpass filter, respectively. Since the location and width of the individual rotational Raman lines are species-specific, the exact level of the rotational Raman scattering signal contribution to the total FRS signal collected by the detector depends on the individual species. For example, calculations for the current experimental conditions show that for N_2 at $T = 296$ K and $P = 1$ atm, approximately 36% and 30% of the Q-branch and Stokes/anti-Stokes rotational Raman scattering signal, respectively, transmit through the I_2 and bandpass filters, while only 22% of the Cabannes line transmits through the filters. This implies that the fractional percent of the rotational Raman scattering component (F_{RR}) increases for FRS as compared to traditional Rayleigh scattering (2% vs 1.4%). For CO_2 at $T = 296$ K and $P = 1$ atm, approximately 44% and 49% of the Q-branch and Stokes/anti-Stokes rotational Raman scattering signal, respectively, transmit through the I_2 and bandpass filters, while only 16% of the Cabannes line signal transmits through the filters and is collected. Thus, for CO_2, there is a significant increase in F_{RR}, increasing from 6% for traditional Rayleigh scattering to 16% for FRS.

The value of F_{RR} can vary as a function of temperature since the Cabannes linewidth, $\mathcal{R}_i(\nu_r)$ and the Raman

linewidths, $\mathcal{R}_i^Q(v_r)$, and $\mathcal{R}_i^{J \to J'}(v_r, \Delta v_{J \to J'})$ can change width (and shape) as a function of gas temperature, while the I_2 lines remain constant for a given I_2 filter cell setting. Figure 12 shows the variation of F_{RR} as a function of temperature for five gases. For all species considered, F_{RR} decreases with increasing temperature. This is due to the fact that the Cabannes linewidth, $\mathcal{R}_i(v_r)$ increases with increasing temperature due to Doppler broadening, while the rotational Raman linewidths remain largely constant due to competing effects of Doppler broadening and collisional broadening. Thus, with increasing temperature, an increasingly larger fraction of the RBS signal (as compared to the rotational Raman scattering signal) transmits through the I_2 filter.

Appendix 2: temperature-dependent values of $c_{int}$and μ_B for combustion-relevant species

Kinetic models of scattered light spectra require collision properties of gases that are used within the collision integral of the Boltzmann equation. For the Tenti S6 model [5], the collision integral is estimated using gas transport properties including the internal specific heat capacity (c_{int}) and the bulk viscosity (μ_B). Both c_{int} and μ_B depend on the relaxation rates of the internal degrees of freedom of the molecule.

Internal specific heat capacity (c_{tint})

In general, the internal specific heat capacity can be calculated as

$$c_{int} = \frac{(5 - 3\gamma)}{2(\gamma - 1)}, \tag{39}$$

where γ is the ratio of specific heats, which can be expressed in terms of the total number of internal degrees of freedom (f), as

$$\gamma = \frac{2}{f} + 1, \tag{40}$$

and thus

$$c_{int} = \frac{(f - 3)}{2}. \tag{41}$$

The total number of degrees of freedom is written as $f = f_t + f_r + f_v$, where $f_t = 3$ is the number of translational degrees of freedom, f_r is the number of rotational degrees of freedom given by

$$f_r = \begin{cases} 2 & \text{linear molecule} \\ 3 & \text{non-linear molecule} \end{cases}, \tag{42}$$

and f_v is the number of vibrational degrees of freedom, given by

$$f_v = \begin{cases} 2(3N - 5) & \text{linear molecule} \\ 2(3N - 6) & \text{non-linear molecule} \end{cases}, \tag{43}$$

where N is the total number of atoms in the molecule. Note, the factor of 2 preceding the parenthetical arguments in Eq. (42) corresponds to the fact that each active vibrational mode has 2° of freedom. Since the number of accessible vibrational modes increases with increasing temperature, $\gamma = \gamma(T)$ and thus the temperature dependence of c_{int} is embedded within γ.

If the relaxation time scale of any internal degree of freedom is much longer than the characteristic time scales of sound propagating through the media, then the internal motion associated with that particular degree of freedom remains frozen on the timescale of the density fluctuations. For light scattering experiments, the characteristic sound frequencies are on the order of 1 GHz and thus internal degrees of freedom with relaxation times scales significantly longer than 1 ns are not active in the light scattering. For N_2, O_2, H_2, CH_4, CO, and CO_2, the vibrational relaxation time scales are longer than 10^{-7} seconds, even at the highest temperatures, and therefore only rotational modes contribute to the scattering. Under these conditions, an effective value of γ (due to rotational motion only) is written as

$$\gamma_r = \frac{f_r + 5}{f_r + 3}, \tag{44}$$

and the internal specific heat capacity is determined as

$$c_{int} = \begin{cases} 1 & \text{linear molecule} \\ 3/2 & \text{non-linear molecule} \end{cases}. \tag{45}$$

For H_2O the vibrational relaxation times range from ~ 10 ns at 300 K to < 1 ns seconds at flame temperatures and cannot be neglected based on timescale arguments. In this manner, c_{int} is calculated in the current work using Eq. (39), where $\gamma = C_p/C_v$ and C_p and C_v are the heat capacity at constant pressure and volume, respectively. The values of C_p are calculated using temperature-dependent polynomial curve fits from Kee et al. [64], and C_v is calculated as $C_v = C_p - R$, where R is the universal gas constant.

When all vibrational modes are active, H_2O has 12 total internal degrees of freedom (3 translational, 3 rotational, and 6 vibrational), which leads to $3/2 \leq c_{int} \leq 9/2$ over a full range of temperatures. The calculation of c_{int} for H_2O using Eq. (39) at any given temperature is an estimation, thus the sensitivity of the synthetic FRS signals to the specified value of c_{int} is assessed. Figure 13 shows calculated synthetic FRS signals from pure H_2O vapor at $P = 1$ atm over the full range of possible values of c_{int} (solid lines) at four different temperatures. The synthetic FRS signals for each value of c_{int} are normalized by the average synthetic FRS signal over the full range of c_{int}
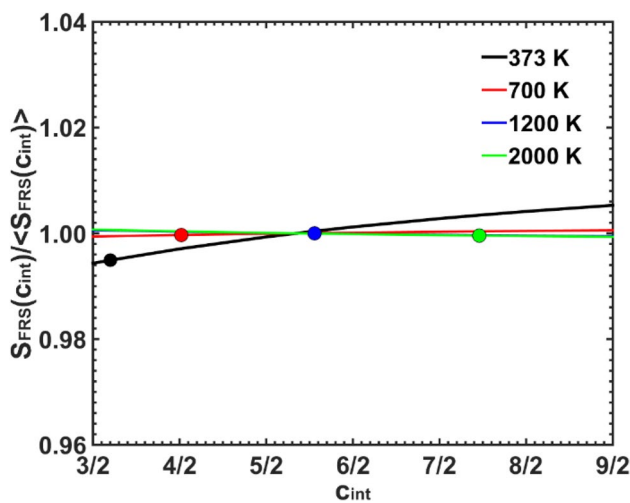
Fig. 13 Variations in calculated water vapor FRS signals at $P = 1$ atm as a function of specified c_{int} values

values. The symbols show the value of c_{int} calculated using Eq. (39) at each temperature. The results show minimal sensitivity of the calculated synthetic FRS signals to the specified value of c_{int} at 1 atm. For example for $T > 700$ K, varying c_{int} over the entire possible range of values results in variations of S_{FRS,H_2O} of less than 0.5%. At higher pressures (or increased y parameter values), the sensitivity of S_{FRS,H_2O} to variations in c_{int} is expected to increase.

Bulk viscosity (μ_B)

Temperature-dependent values of the bulk viscosity can be estimated from relaxation time measurements found within the literature. Assuming that rotational and vibrational modes relax independently, each with a single time scale, the bulk viscosity can be written as

$$\mu_B = \mu_{B,r} + \mu_{B,v}, \tag{46}$$

where $\mu_{B,r}$ and $\mu_{B,v}$ are the rotational and vibrational contributions to the bulk viscosity and given by the following expressions:

$$\mu_{B,r} = (\gamma - 1)^2 \frac{f_r}{2} p \tau_r, \tag{47}$$

$$\mu_{B,v} = (\gamma - 1)^2 \left(\frac{Cv}{R} - \frac{f_r + 3}{2} \right) p \tau_v, \tag{48}$$

where p is the pressure, τ_r is the rotational relaxation time, and τ_v is the vibrational relaxation time. As discussed above, when the vibrational relaxation times are long compared to the characteristic time scale of the density fluctuations, there is no vibrational–translational energy exchange and the vibrational modes are assumed to be "frozen". For N_2, O_2, H_2, CH_4, CO, and CO_2, it is assumed that only rotation contributes to μ_B and the bulk viscosity is calculated using Eq. (47) with γ_r replacing γ. For water vapor, both rotational and vibrational contributions are included and Eqs. (46)–(48) are used to calculate the bulk viscosity. The rotational and vibrational relaxation times for the considered species at various temperatures are taken from sources within the literature as reported in Table 2. The values of $p\tau_r$ and $p\tau_v$ are fit to either power law or logarithmic expressions that serve as convenient fits to the data. There is sufficient relaxation time data for all species at room temperature, but for many species the relaxation time data are sparse at higher temperatures. For these cases, existing bulk viscosity models were used to help guide the choice of fit (power law or logarithmic), but not used as data to determine the fit. When compiling all the entirety of the relaxation rates, $p\tau_r$ and $p\tau_v$ (for water vapor) were fit to

$$p\tau = AT^B + C \ln T + D . \tag{49}$$

Table 2 Temperature-dependent species properties

Coefficients for p_τ Eq. (49)									
Species	c_{int}	A	B	C	D	μ_B/μ at 300 K	Refs.[a]	T(K) range, data	T(K) range, Eq. (24)[b]
N_2	1	4.23e−8	1.327	0	0	0.74	[65–69]	77–1555	77–2000
O_2	1	0	0	3.47e−4	−1.92e−3	0.63	[66–68]	295–1073	295–2000
H_2	1	1.55e−5	0.823	0	0	30.3	[67, 70]	295–1900	295–2000
CO	1	1.73e−7	0.998	0	0	0.46	[65, 66, 71–74]	260–580	260–2200
CH_4	3/2	1.75e−9	1.931	0	0	1.54	[65, 75–77]	293–773	293–1100
CO_2	1	7.09e−9	1.456	0	0	0.30	[66, 68, 78–81]	284–676	280–1600
H_2O	Varies	0	0	3.57e−4	−2.03e−3	2.1	[50, 51, 82, 83]	323–940	295–1600
	Equation (13)	0	0	6.55e+1	−1.85e00			373–2915	295–3000

[a]Relaxation time data used in the fit of Eq. (49)

[b]The applicable temperature range of the temperature fit (Eq. 49) is determined using a combination of the experimental data and a comparison of the qualitative shape of the temperature fit and existing models found within the literature
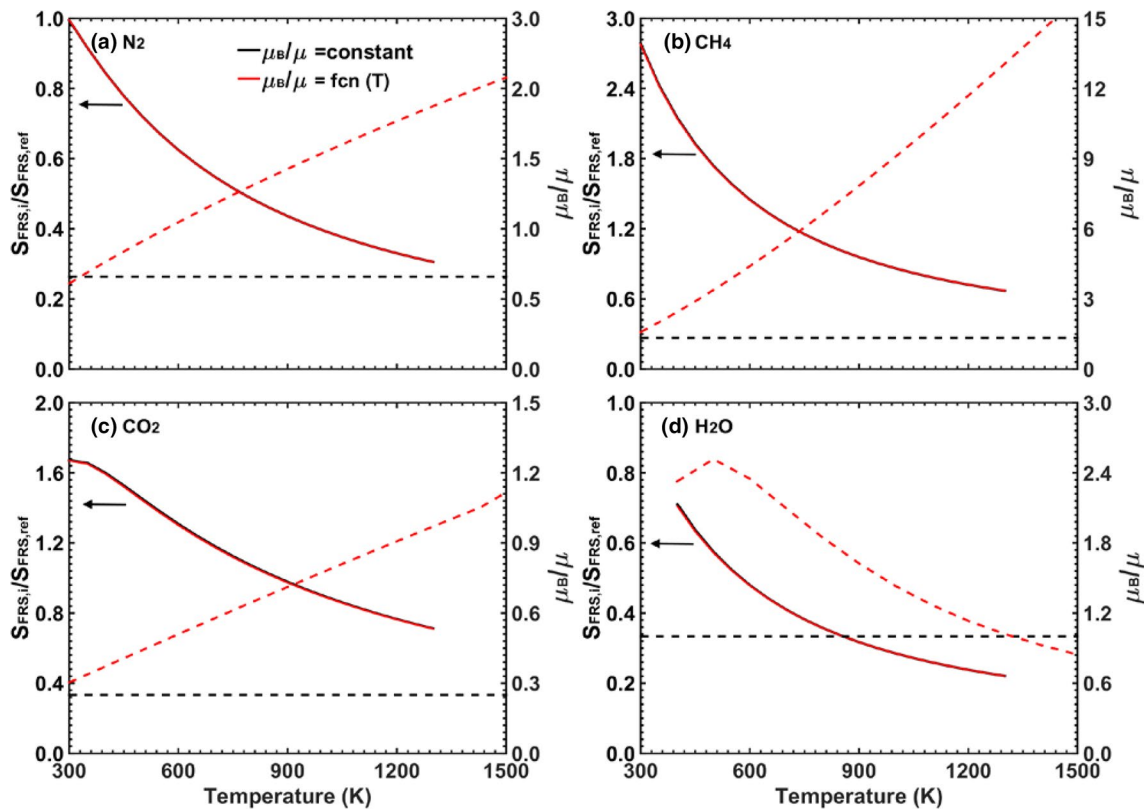
Fig. 14 Normalized synthetic FRS signal curves as a function of temperature for constant μ_B/μ (solid black line) and a temperature-dependent value of μ_B/μ (solid red line) according to Eqs. (46)–(49).

The ratio of μ_B/μ for each calculation is given as the dashed lines and shown on the secondary y-axis. The reference condition is N_2 at $T = 296$ K

Table 2 lists the constants for each species, the range of temperatures in which relaxation times were obtained, and the suggested range of temperatures over which the fit of Eq. (49) is valid. For H_2O, the first row of constants correspond to $p\tau_r$ and the second row of constants correspond to $p\tau_v$. Table 2 also lists the calculated values of μ_B/μ at 300 K. For N_2, O_2, H_2, CH_4, CO, and CO_2, the values of μ_B/μ derived from Eqs. (47) and (49) compare very favorably with those reported within the literature, including the values inferred from direct measurements of the RBS spectra. For example, the current fit yields a value of $\mu_B/\mu = 0.74$ for N_2, while Gu et al. [14] and Gu and Ubachs [13] determined $\mu_B/\mu = 0.79$ at room temperature. For CO_2, the current fit yields a value of $\mu_B/\mu = 0.30$, while Pan et al. [48], Lao et al. [52], Meijer et al. [53], and Gu et al. [12] determined $\mu_B/\mu = 0.25$, 0.31, 0.39, and 0.38, respectively.

Because of the limited amount of bulk viscosity data, it is not possible to evaluate the accuracy of the temperature-dependent expressions for μ_B at elevated temperatures. Figure 14 shows example synthetic FRS signals as a function of temperature for four different species, N_2, CH_4, CO_2, and H_2O using (1) a constant μ_B/μ ratio determined at room temperature (solid black line), implying that the temperature

dependence of μ_B is exactly that of μ and (2) a temperature-dependent μ_B/μ ratio (solid red line), where μ_B is determined using Eqs. (46)–(49). In Fig. 14, the values of μ_B/μ are shown with dashed lines. The results shown in Fig. 14 indicate little observable difference between the synthetic FRS signals calculated with the two different sets of μ_B/μ values, even when there are significant differences in μ_B as is the case for CH_4.

To further investigate the sensitivity of the synthetic FRS signals to the chosen value of μ_B, the synthetic FRS signals are calculated for all species as a function of temperature for varying values of μ_B The percent difference between the synthetic FRS signal calculated with an arbitrary value of the bulk viscosity, μ_B^*, and the synthetic FRS signal calculated with the bulk viscosity determined using Eqs. (46)–(49) is defined by

$$\epsilon_{\mu_B} = \frac{\left| S_{\text{FRS}}(\mu_B^*) - S_{\text{FRS}}(\mu_B) \right|}{S_{\text{FRS}}(\mu_B)}. \tag{50}$$

Figure 15 shows the results of varying the value of the bulk viscosity by a factor of 100 ($0.1 \leq \mu_B^*/\mu \leq 10$) for temperatures of 300 K, 700 K, 1200 K, and 2000 K. For higher
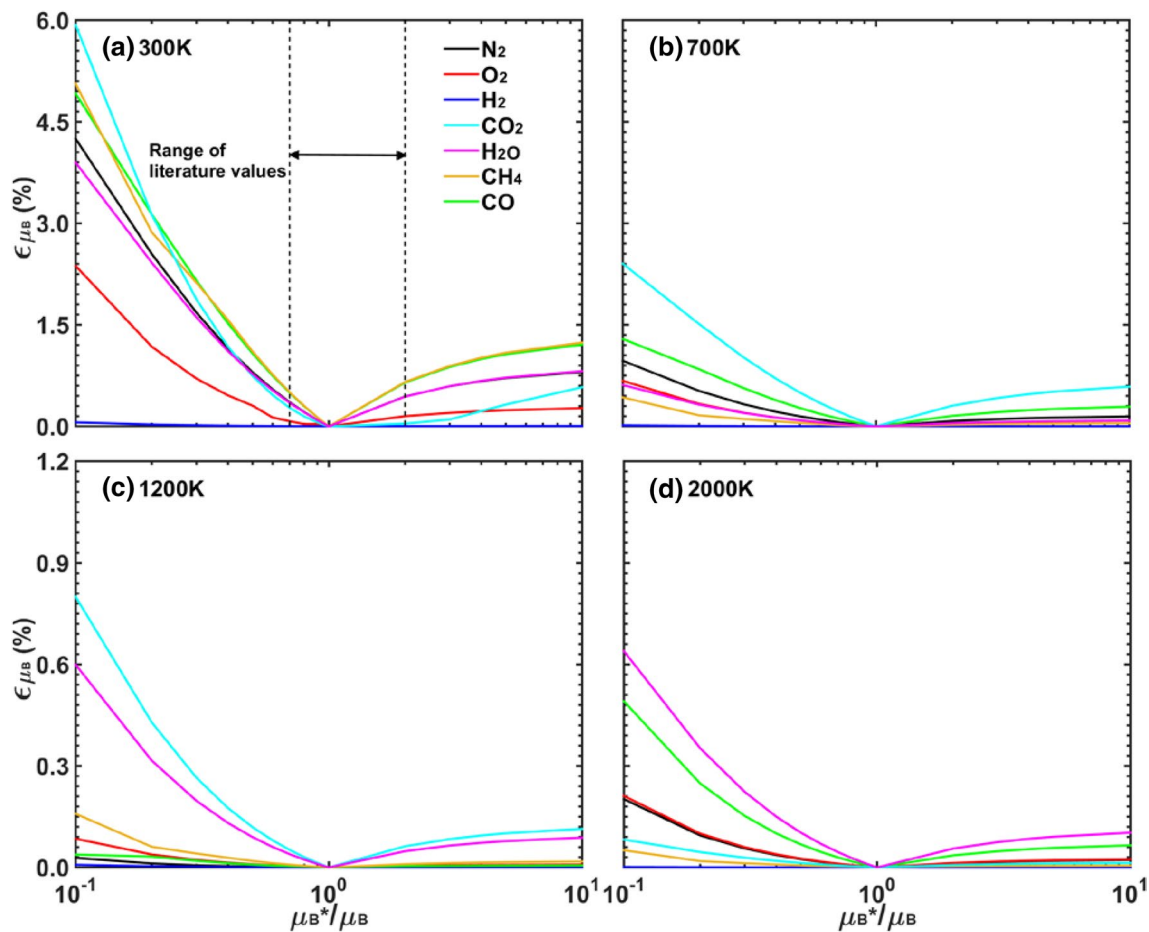
Fig. 15 Sensitivity of the synthetic FRS signals to changes in values of bulk viscosity for **a** $T = 300$ K, **b** $T = 700$ K, **c** $T = 1200$ K, and **d** $T = 2000$ K

temperatures ($T \geq 700$ K), the variation of the bulk viscosity leads to negligible variations in the calculated FRS signal over the full range of bulk viscosities tested. Only at room temperature ($T = 300$ K), do very small values of the bulk viscosity lead to notable changes in the calculated FRS signal. However, over the range of bulk viscosities reported within the literature, variations in μ_B lead to changes in the synthetic FRS signal by less than 1%. Overall, the results shown in Figs. 14 and 15 demonstrate that the calculated FRS signal is insensitive to the value of bulk viscosity, as long as μ_B does not approach zero. However, it should be noted that the FRS signal will likely become increasingly sensitive to the values of μ_B as pressure (y parameter) increases.

References

1. J.W. Strutt, On the transmission of light through an atmosphere containing small particles in suspension, and on the origin of the blue of the sky. The London, Edinburgh, and Dublin Philosophical Magazine and. J. Sci. **47**, 375–384 (1899)
2. R.W. Boyd, *Nonlinear Optics*, 3rd ed. (Academic Press, Cambridge, 2008)
3. A.T. Young, Rayleigh scattering. Appl. Opt. **20**, 533–535 (1981)
4. C.D. Boley, R.C. Desai, G. Tenti, Kinetic models and Brillouin scattering in a molecular gas. Can. J. Phys. **50**, 2158–2173 (1972)
5. G. Tenti, C.D. Boley, R.C. Desai, On the kinetic model description of Rayleigh–Brillouin scattering from molecular gases. Can. J. Phys. **52**, 285–290 (1974)
6. C.S. Wang Chang, G.E. Uhlenbeck, J. de Boer, The heat conductivity and viscosity of poly-atomic gases. in *Studies in Statistical Mechanics*, ed. by J. deBoer, G.E. Uhlenbeck (Wiley, New York, 1964)
7. A. Stoffelen, G.J. Marseille, F. Bouttier, D. Vasiljevic, S. De Haan, C. Cardinali, ADM-aeolus doppler wind lidar observing system simulation experiment. Q. J. R. Meteorol. Soc. 132, 1927–1947 (2006)
8. B. Witschas, C. Lemmerz, O. Reitebuch, Daytime measurements of atmospheric temperature profiles (2–15 km) by lidar utilizing Rayleigh–Brillouin scatterin. Opt. Lett. **39**, 1972–1975 (2014)
9. M.O. Vieitez, E.J. van Duijn, W. Ubachs, B. Witschas, A. Meijer, A.S. de Wijn, N.J. Dam, W. van de Water, Coherent and spontaneous Rayleigh–Brillouin scattering in atomic and molecular gases and gas mixtures. Phys. Rev. A **82**, 043836 (2010)

10. Y. Ma, H. Li, Z. Gu, W. Ubachs, Y. Yu, J. Huang, B. Zhou, Y. Wang, K. Liang, Analysis of Rayleigh–Brillouin spectral profiles and Brillouin shifts in nitrogen gas and ai. Opt. Express **22**, 2092–2104 (2014)

11. B. Witschas, M.O. Vieitez, E.-J. van Duijn, O. Reitebuch, W. van de Water, W. Ubachs, Spontaneous Rayleigh–Brillouin scattering of ultraviolet light in nitrogen, dry air, and moist ai. Appl. Opt. **49**, 4217–4227 (2010)

12. Z.Y. Gu, W. Ubachs, W. van de Water, Rayleigh–Brillouin scattering of carbon dioxide. Opt. Lett. **39**, 3301–3304 (2014)

13. Z. Gu, W. Ubachs, A systematic study of Rayleigh–Brillouin scattering in air, N2, and O$_2$ gases. J. Chem. Phys. **141**, 104320 (2014)

14. Z. Gu, B. Witschas, W. van de Water, W. Ubachs, Rayleigh–Brillouin scattering profiles of air at different temperatures and pressure. Appl. Opt. **52**, 4640–4651 (2013)

15. J.N. Forkey, W.R. Lempert, R.B. Miles, Accuracy limits for planar measurements of flow field velocity, temperature and pressure using Filtered Rayleigh Scatterin. Exp. Fluids **24**, 151–162 (1998)

16. R.B. Miles, W.R. Lempert, J.N. Forkey, Laser Rayleigh scattering. Meas. Sci. Technol. **12**, R33 (2001)

17. M. Boguszko, G.S. Elliott, On the use of filtered Rayleigh scattering for measurements in compressible flows and thermal field. Exp. Fluids **38**, 33–49 (2005)

18. U. Doll, G. Stockhausen, C. Willert, Pressure, temperature, and three-component velocity fields by filtered Rayleigh scattering velocimetr. Opt. Lett. **42**, 3773–3776 (2017)

19. U. Doll, G. Stockhausen, C. Willert, Endoscopic filtered Rayleigh scattering for the analysis of ducted gas flows. Exp. Fluids **55**, 1690 (2014)

20. F. Benhassen, M.D. Polanka, M.F. Reeder, Trajectory measurements of a horizontally oriented buoyant jet in a coflow using filtered rayleigh scattering. J. Aerosp. Eng. **30**, 04016067 (2017)

21. J. Brübach, J. Zetterberg, A. Omrane, Z.S. Li, M. Aldén, A. Dreizler, Determination of surface normal temperature gradients using thermographic phosphors and filtered Rayleigh scatterin. Appl. Phys. B **84**, 537–541 (2006)

22. P.M. Allison, T.A. McManus, J.A. Sutton, Quantitative fuel vapor/air mixing imaging in droplet/gas regions of an evaporating spray flow using filtered Rayleigh scattering. Opt. Lett. **41**, 1074–1077 (2016)

23. D. Hoffman, K.U. Münch, A. Leipertz, Two-dimensional temperature determination in sooting flames by filtered Rayleigh scattering. Opt. Lett. **21**, 525–527 (1996)

24. G. Elliott, N. Glumac, C. Carter, Molecular filtered Rayleigh scattering applied to combustion. Meas. Sci. Technol. **12**, 452 (2001)

25. D. Most, A. Leipertz, Simultaneous two-dimensional flow velocity and gas temperature measurements by use of a combined particle image velocimetry and filtered Rayleigh scattering technique. Appl. Opt. **40**, 5379–5387 (2001)

26. D. Most, F. Dinkelacker, A. Leipertz, Direct determination of the turbulent flux by simultaneous application of filtered rayleigh scattering thermometry and particle image velocimetry. Proc. Comb. Inst. **29**, 2669–2677 (2002)

27. A.P. Yalin, Y.Z. Ionikh, R.B. Miles, Gas temperature measurements in weakly ionized glow discharges with filtered Rayleigh scattering. Appl. Opt. **41**, 3753–3762 (2002)

28. S.P. Kearney, R.W. Schefer, S.J. Beresh, T.W. Grasser, Temperature imaging in nonpremixed flames by joint filtered Rayleigh and Raman scattering. Appl. Opt. **44**, 1548–1558 (2005)

29. J.R. Bonatto, W. Marques Jr., Kinetic model analysis of light scattering in binary mixtures of monatomic ideal gases. J. Stat. Mech. **2005**, P09014–P09014 (2005)

30. A.S. Fernandes, W. Marques, Sound propagation in binary gas mixtures from a kinetic model of the Boltzmann equation. Phys. A **332**, 29–46 (2004)

31. W. Marques, Coherent Rayleigh–Brillouin scattering in binary gas mixtures. J. Stat. Mech. **2007**, 03013–03013 (2007)

32. L. Letamendia, Light-scattering studies of moderately dense gas mixtures: Hydrodynamic regime. Phys. Rev. A Gen. Phys. **24**, 1574–1590 (1981)

33. L. Letamendia, P. Joubert, J.P. Chabrat, J. Rouch, C. Vaucamps, C.D. Boley, S. Yip, S.H. Chen, Light-scattering studies of moderately dense gases. II. Nonhydrodynamic regime. Phys. Rev. A **25**, 481–488 (1982)

34. J.N. Forkey, W.R. Lempert, R.B. Miles, Corrected and calibrated I_2 absorption model at frequency-doubled Nd:YAG laser wavelengths. Appl. Opt. **36**, 6729–6738 (1997)

35. T.L. Labus, E.P. Symons, Experimental investigation of an axisymmetric free jet with an initially uniform velocity profile, NASA Technical Report NASA-TN-D-6783, E-6801 (1972)

36. J. Gauntner, P. Hrycak, D. Lee, J. Livingood, Experimental flow characteristics of a single turbulent jet impinging on a flat plate, NASA Technical Report NASA-TN D-5690 (1970)

37. M.W. Thring, M.P. Newby, Combustion length of enclosed turbulent jet flames. Sym. (Int.) Combust. **4**, 789–796 (1953)

38. K.M. Tacina, W.J. Dahm, Effects of heat release on turbulent shear flows. Part 1. A general equivalence principle for non-buoyant flows and its application to turbulent jet flames. J. Fluid Mech. **415**, 23–44 (2000)

39. R.D. Hancock, K.E. Bertagnolli, R.P. Lucht, Nitrogen and hydrogen CARS temperature measurements in a hydrogen/air flame using a near-adiabatic flat-flame burner. Combust. Flame **109**, 323–331 (1997)

40. M.J. Papageorge, C. Arndt, F. Fuest, W. Meier, J.A. Sutton, High-speed mixture fraction and temperature imaging of pulsed, turbulent fuel jets auto-igniting in high-temperature, vitiated co-flows. Exp. Fluids **55**, 1763 (2014)

41. J.A. Sutton, J.F. Driscoll, Rayleigh scattering cross sections of combustion species at 266, 355, and 532 nm for thermometry application. Opt. Lett. **29**, 2620–2622 (2004)

42. C. Carter, *Laser-based Rayleigh and Mie scattering methods* (Wiley, New York, 1996), pp. 1078–1093

43. R.L. McKenzie, Measurement capabilities of planar Doppler velocimetry using pulsed lasers. Appl. Opt. **35**, 948–964 (1996)

44. R. Patton, J. Sutton, Seed laser power effects on the spectral purity of Q-switched Nd:YAG lasers and the implications for filtered rayleigh scattering measurements. Appl. Phys. B Lasers Opt. **111**, 457–468 (2013)

45. J.A. Sutton, R.A. Patton, Improvements in filtered Rayleigh scattering measurements using Fabry–Perot etalons for spectral filtering of pulsed, 532-nm Nd:YAG output. Appl. Phys. B **116**, 681–698 (2014)

46. P. Linstrom, W. Mallard, Nist standard reference database number 69 (2003), 2018

47. B.J. McBride, S. Gordon, M.A. Reno, Coefficients for calculating thermodynamic and transport properties of individual species, NASA Technical Report NASA-TM-4513, E-7981 (1993)

48. X. Pan, M.N. Shneider, R.B. Miles, Coherent Rayleigh–Brillouin scattering in molecular gases. Phys. Rev. A **69**, 033814 (2004)

49. J.D. Lambert, *Vibrational and rotational relaxation in gases* (Oxford University Press, Oxford, 1977)

50. H.E. Bass, J.R. Olson, R.C. Amme, Vibrational relaxation in H_2O vapor in the temperature range 373–946 K. J. Acoust. Soc. Am. **56**, 1455–1460 (1974)

51. R. Kung, R. Center, High temperature vibrational relaxation of H_2O by H_2O, He, Ar, and N2. J. Chem. Phys. **62**, 2187–2194 (1975)

52. Q. Lao, P. Schoen, B. Chu, Rayleigh–Brillouin scattering of gases with internal relaxation. J. Chem. Phys. **64**, 3547–3555 (1976)

53. A. Meijer, A. de Wijn, M. Peters, N. Dam, W. van de Water, Coherent Rayleigh–Brillouin scattering measurements of bulk viscosity of polar and nonpolar gases, and kinetic theory. J. Chem. Phys. **133**, 164315 (2010)

54. M.S. Cramer, Numerical estimates for the bulk viscosity of ideal gases. Phys. Fluids **24**, 066102 (2012)

55. S.P. Kearney, S.J. Beresh, T.W. Grasser, R.W. Schefer, P.E. Schrader, R.L. Farrow, A filtered rayleigh scattering apparatus for gas-phase and combustion temperature imaging. Paper AIAA 2003 – 584, 41st Aerospace Sciences Meeting, Reno, NV, January 2003

56. G.K. Wertheim, M.A. Butler, K. West, D.N.E. Buchanan, Determination of the Gaussian and Lorentzian content of experimental line shapes. Rev. Sci. Instrum. **45**(11), 1369–1371 (1974)

57. T. Ida, M. Ando, H. Toraya, Extended pseudo-Voigt function for approximating the Voigt profile. J. Appl. Crystallogr. **33**(6), 1311–1316 (2000)

58. C.M. Penney, R.L. St. Peters, M. Lapp, Absolute rotational Raman cross sections for N_2, O_2, and CO_2. J. Opt. Soc. Am. **64**(5), 712–716 (1974)

59. A. Weber, in *The Raman Effect, vol 2: Applications*, ed. by A. Anderson (Dekker, New York, 1973) **(Ch. 9)**

60. G. Herzberg, *Molecular Spectra and Molecular Structure I. Spectra of Diatomic Molecules* (Van Nostrand, Princeton, 1950)

61. M.P. Bogaard, A.D. Buckingham, R.K. Pierens, A.H. White, Rayleigh scattering depolarization ratio and molecular polarizability anisotropy for gases. J. Chem. Soc. Faraday Trans. 1 Phys. Chem. Condensed Phases **74**, 3008–3015 (1978)

62. K.S. Jammu, G.E. St. John, H.L. Welsh, Pressure broadening of the rotational raman lines of some simple gases. Can. J. Phys. **44**(4), 797–814 (1966)

63. J.W. Gallagher, R.D. Johnson, in *NIST Chemistry WebBook, NIST Standard Reference Database Number 69*, ed. by P.J. Linstrom, W.G. Mallard. Constants of Diatomics Molecules (National Institute of Standards and Technology, Gaithersburg). https://doi.org/10.18434/T4D303. Accessed 6 Nov 2018

64. R. Kee, F. Rupley, J. Miller, M. Coltrin, J. Grcar, E. Meeks, H. Moffat, A. Lutz, G. Dixon-Lewis, M. Smooke, *CHEMKIN Collection, Release 3.6* (Reaction Design, Inc, San Diego, 2000)

65. G. Prangsma, A. Alberga, J. Beenakker, Ultrasonic determination of the volume viscosity of N_2, CO, CH_4 and CD_4 between 77 and 300 K. Physica **64**, 278–288 (1973)

66. B. Annis, A. Malinauskas, Temperature dependence of rotational collision numbers from thermal transpiration. J. Chem. Phys. **54**, 4763–4768 (1971)

67. T.G. Winter, G.L. Hill, High-temperature ultrasonic measurements of rotational relaxation in hydrogen, deuterium, nitrogen, and oxygen. J. Acoust. Soc. Am. **42**, 848–858 (1967)

68. R. Healy, T. Storvick, Rotational collision number and Eucken factors from thermal transpiration measurements. J. Chem. Phys. **50**, 1419–1427 (1969)

69. M. Camac, Avco Everett Research Laboratory. Research Report 172 (1963)

70. R.J. Gallagher, J.B. Fenn, Rotational relaxation of molecular hydrogen. J. Chem. Phys. **60**, 3492–3499 (1974)

71. A.D. Gupta, T. Storvick, Analysis of the heat conductivity data for polar and nonpolar gases using thermal transpiration measurements. J. Chem. Phys. **52**, 742–749 (1970)

72. J. Tao, G. Ganzi, S. Sandler, Determination of thermal transport properties from thermal transpiration measurements. II. J. Chem. Phys. **56**, 3789–3793 (1972)

73. J. Tao, W. Revelt, S. Sandler, Determination of thermal transport properties from thermal transpiration measurements. III. Polar gases. J. Chem. Phys. **60**, 4475–4482 (1974)

74. M.J. Assael, W.A. Wakeham, Thermal conductivity of four polyatomic gases. J. Chem. Soc. Faraday Trans. 1 Phys. Chem. Condensed Phases **77**, 697–707 (1981)

75. G. Hill, T. Winter, Effect of temperature on the rotational and vibrational relaxation times of some hydrocarbons. J. Chem. Phys. **49**, 440–444 (1968)

76. P. Kistemaker, M. Hanna, A. Tom, A. De Vries, Rotational relaxation in mixtures of methane with helium, argon and xenon. Physica **60**, 459–471 (1972)

77. R. Holmes, G. Jones, N. Pusat, Combined viscothermal and thermal relaxation in polyatomic gases. Trans. Faraday Soc. **60**, 1220–1229 (1964)

78. A. Malinauskas, Thermal transpiration. rotational relaxation numbers for nitrogen and carbon dioxide. J. Chem. Phys. **44**, 1196–1202 (1966)

79. A. Tip, J. Los, A. De Vries, Rotational relaxation numbers from thermal transpiration measurements. Physica **35**, 489–498 (1967)

80. C. O'Neal Jr., R.S. Brokaw, Relation between thermal conductivity and viscosity for nonpolar gases. II. Rotational relaxation of polyatomic molecules. Phys. Fluids **6**, 1675–1682 (1963)

81. E. Mason, Molecular relaxation times from thermal transpiration measurements. J. Chem. Phys. **39**, 522–526 (1963)

82. R.G. Keeton, H. Bass, Vibrational and rotational relaxation of water vapor by water vapor, nitrogen, and argon at 500 K. J. Acoust. Soc. Am. **60**, 78–82 (1976)

83. H. Roesler, K.F. Sahm, Vibrational and rotational relaxation in water vapor. J. Acoust. Soc. Am. **37**, 386–387 (1965)